Characterization of UV-light curable piezoelectric 0-0-3 composites filled with lead-free ceramics and conductive nanoparticles: supplementary material

1. MATERIALS AND METHODS

A. Materials. Ceramic particles

In total two different lead-free piezoelectric ceramics, Barium titanate (BTO) (purchased from Nanografi Nanotechnology AS, Çankaya/Ankara, Turkey) and Sodium potassium niobate (KNN) (purchased from Nippon Chemical Industrial Co., Ltd., Tokyo, Japan) are investigated in this study. Two particle sizes of each ceramic are available, therefore, in total four piezoelectric ceramics are investigated. Ceramic materials are further named BTO7, BTO13, KNN3, and KNN6 with respect to their mean particle sizes. Scanning Electron Microscopy (SEM) images of the ceramics as received (Fig. S1) and X-ray diffraction (XRD) data of the ceramics as received (Fig. S2) are shown below. Properties of the ceramics are listed in Table S1. Refractive indexes, piezoelectric charge coefficients d_{33}, relative permittivities, dielectric losses, and coercive fields of ceramics were not measured in this study and are taken from the literature. Ceramic content in the piezoelectric composites investigated in this study was always kept constant at 30 vol.%.

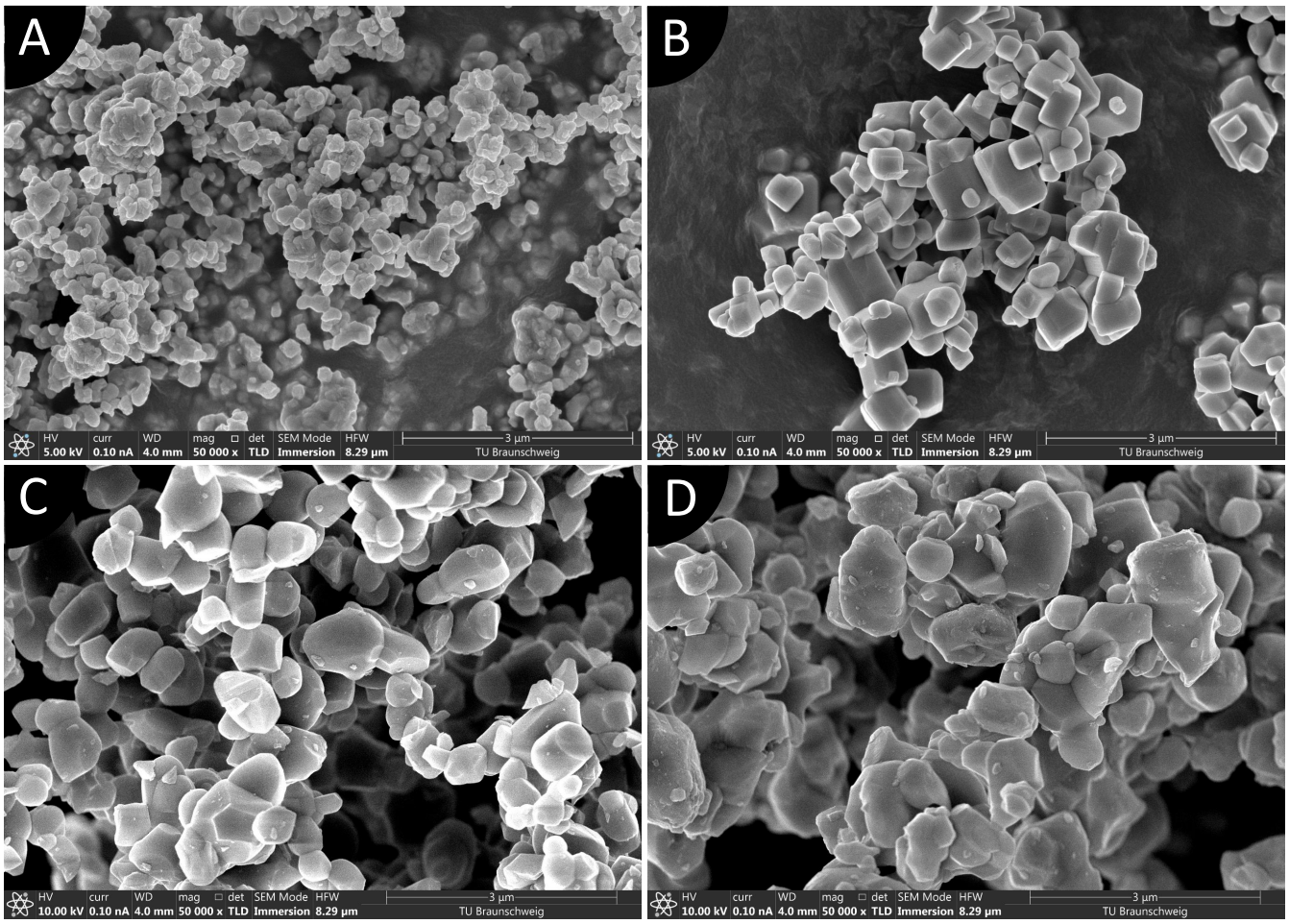

Fig. S1. SEM images of piezoelectric ceramics used in this study ($\times 50,000$): (A) KNN3; (B) KNN6; (C) BTO7; (D) BTO13.

Table S1. Properties of piezoelectric ceramics.

Property	KNN3	KNN6	BTO7	BTO13
Particle size from SEM [μm]	0.326±0.130	0.629±0.227	0.675±0.258	1.346±0.436
Particle size deviation [%]	(39.8%)	(36%)	(38.2%)	(32.3%)
Particle geometry	Random	Cubic	Oval/spherical	Oval/spherical
Theoretical density [1] [g/cm^3]	4.2	4.2	6.02	6.02
Refractive index [2]	2.3-2.4 [3]	2.3-2.4 [3]	2.37-2.64 [4]	2.37-2.64 [4]
Piezoelectric charge coefficient d_{33} [5] [pC/N]	80 [6]	80 [6]	190 [7]	190 [7]
Relative permittivity [5] [-]	290 [6]	290 [6]	1700 [7]	1700 [7]
Dielectric loss [5] [-]	0.04 [6]	0.04 [5]	0.01 [7]	0.01 [7]
Coercive field [5] [kV/mm]	>0.6 [8]	>0.6 [8]	0.4 [7]	0.4 [7]

[1] theoretical densities of the ceramics were used for composite weighting calculations and are taken from literature; [2] at 405nm wavelength, room temperature. Taken from literature and were not measured in this study; [3] Source: [1]; [4] Sources: [2, 3]; [5] Taken from literature and were not measured in this study; [6] Source: [4]; [7] Sources: [5, 6]; [8] Source: [7].

Ceramic particle sizes were measured from SEM images (at x20 000) using Digimizer software (MedCalc Software Ltd, Ostend, Belgium) and measuring at least 30 particles for every ceramic. SEM images were made with Helios G4 CX DualBeam™ (Thermo Fisher Scientific, Waltham, MA, United States). From SEM images of ceramics (Fig. S1), both BTO ceramics show oval/spherical particle geometry, while some particles have sharp edges. Particle size distribution is not high, but both ceramics contain very small ceramic particles (<100 nm) that were not taken into account when measuring particle size. Some BTO particles are partially sintered together. KNN3 ceramic particles show irregular geometry, particles are partially sintered together. On the other hand, KNN6 has a very clear cubic geometry with a few particles showing irregular geometry.

The XRD results are presented in Fig S2. XRD pattern of KNN6 particles shows similarities to orthorhombic KNN patterns reported in the literature [8–12] which has piezoelectric properties. The intensity ratio between (220)/(002) peaks at about 1.52 also suggests a highly orthorhombic lattice structure [11]. KNN3 shows peaks at very similar 2θ degrees in XRD patterns, however, the peaks are lower compared to KNN6. A decrease in the ratio between (220)/(002) peaks (a decrease from 1.52 to 1.1) suggests some co-existence of both orthorhombic and tetragonal phases [11], where both of them are piezoelectric.

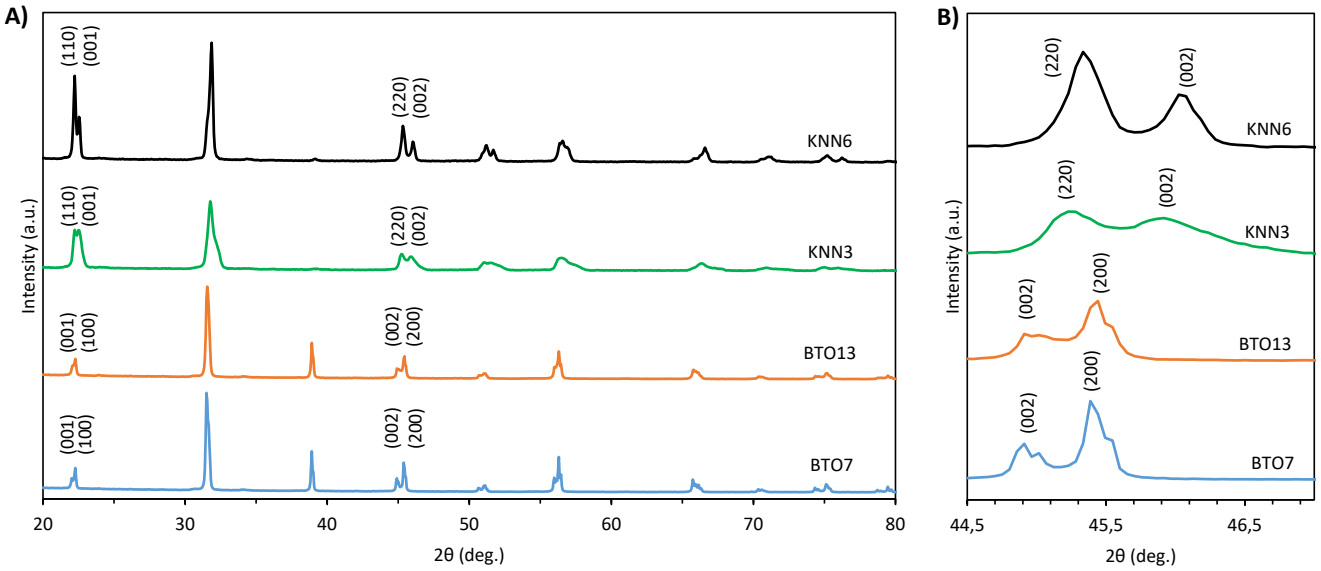

Fig. S2. X-ray diffraction pattern at room temperature of ceramics used in this study: (A) Full graph; (B) Enlarged peaks between 2θ 44.5° and 47°.

XRD pattern of BTO ceramic reveals splitting (002)/(200) peaks which suggests BTO has a tetragonal structure [13], where

the peak intensity ratio (002/200) close to 1:2 for both BTO ceramics is in agreement with the literature, indicating tetragonal BTO structure [14–16]. The sharpness of the peaks also suggests good crystallinity for BTO7 and KNN6 ceramics [13]. Therefore, all four ceramics used in this study are piezoelectric.

B. Materials. Conductive Nanofillers

Four types of different conductive nanofillers are used in this study: COOH (carboxylic acid) - functionalized Multi-Walled Carbon nanotubes (MWCNTs) (purchased from FutureCarbon GmbH, Bayreuth, Germany), Graphene Nanoplatelets (GNPs) (purchased from IoLiTec-Ionic Liquids Technologies GmbH, Heilbronn, Germany), Graphene oxide (GO2) and Graphene oxide (GO3) (both graphene oxides purchased from The Sixth Element (Changzhou) Materials Technology Co., Ltd., Jiangsu, China). All nanofillers have been used as received without further chemical modifications. Their properties (Table S2) and microstructure - SEM images of nanomaterials (Fig. S3-S6).

Table S2. Properties of nanofillers.

Property	MWCNTs[1]	GNPs[2]	GO2[3]	GO3[3]
Manufacturer reference	MWCNTs (COOH-functionalized)	CP-0081-HP-0100	SE1232	SE1233-S
Surface area, m^2/g	≈ 110	≈ 750	≈ 285	≈ 504

[1] MWCNTs - Multi Wall Carbon Nanotubes;
[2] GNPs - Graphene nanoplatelets;
[3] GO - Graphene oxide;

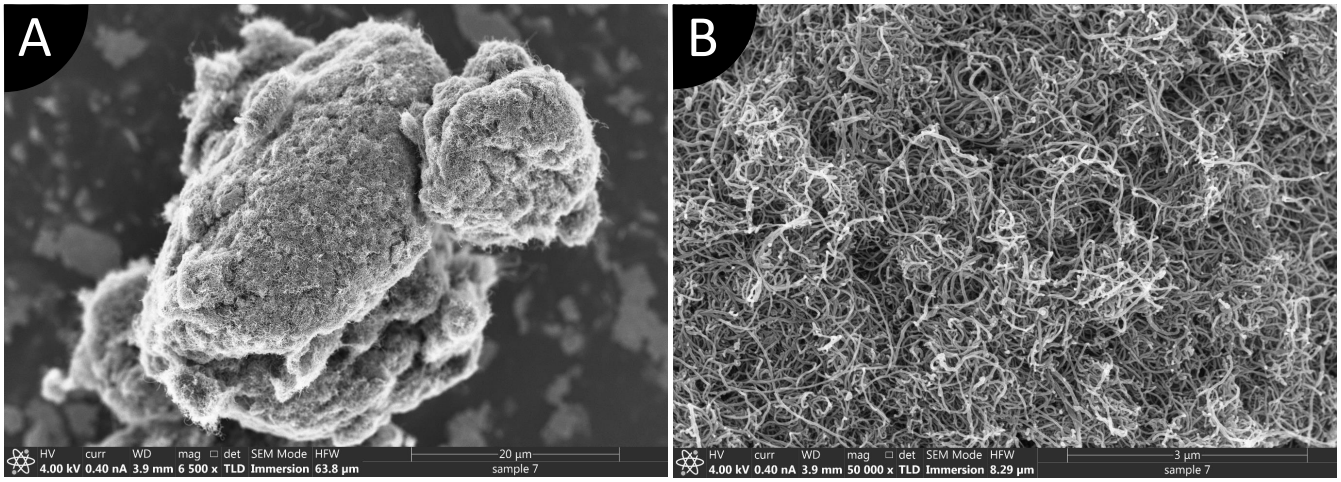

Fig. S3. SEM images of MWCNTs: (A) ($\times 6,500$); (B) ($\times 50,000$).

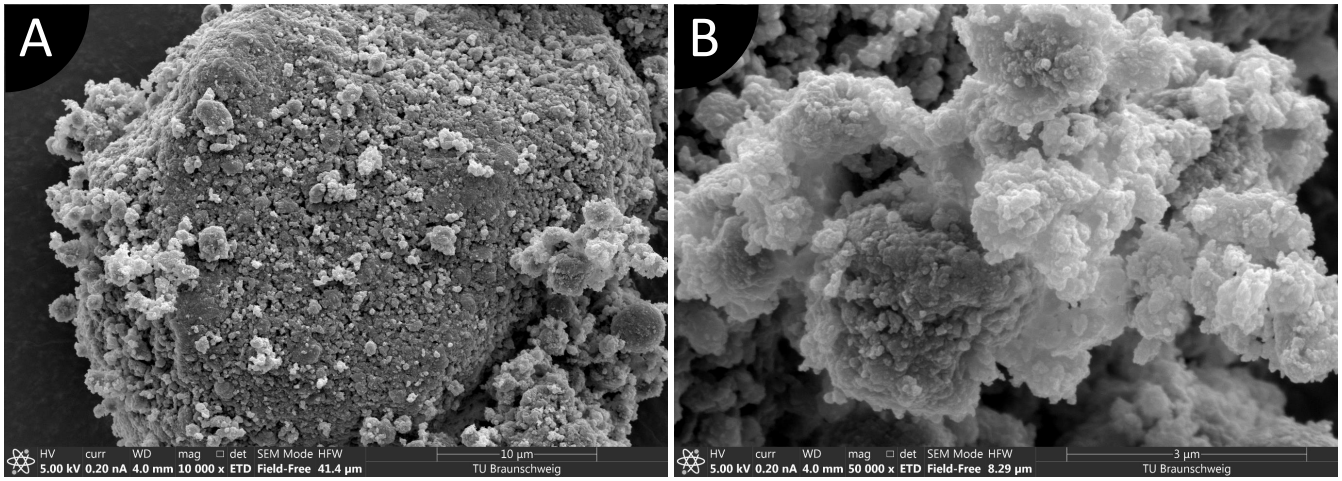

Fig. S4. SEM images of GNPs: (A) ($\times 10,000$); (B) ($\times 50,000$).

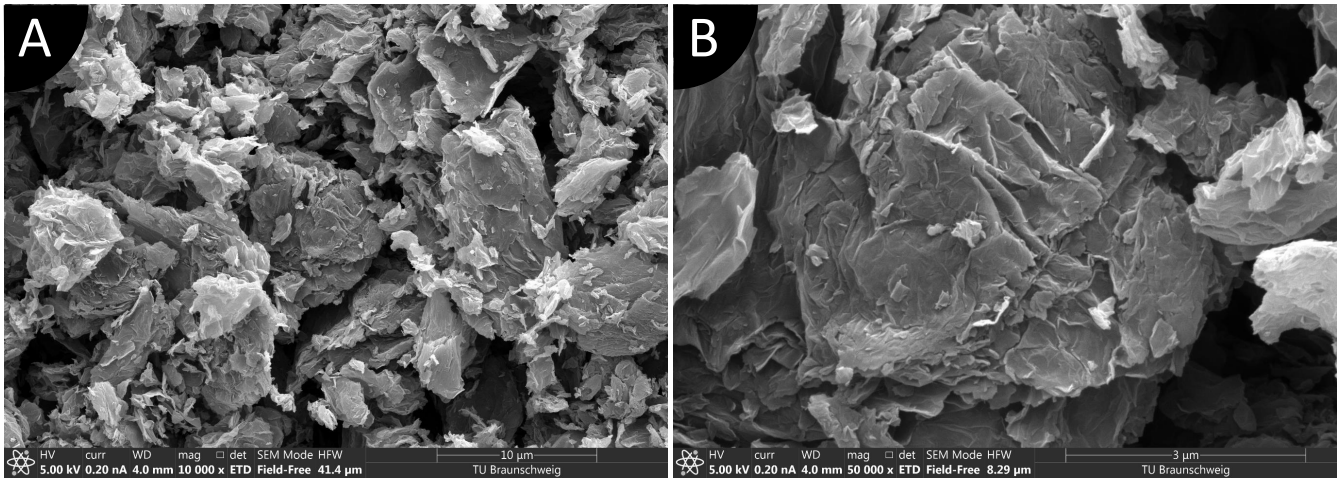

Fig. S5. SEM images of GO2: (A) ($\times 10,000$); (B) ($\times 50,000$).

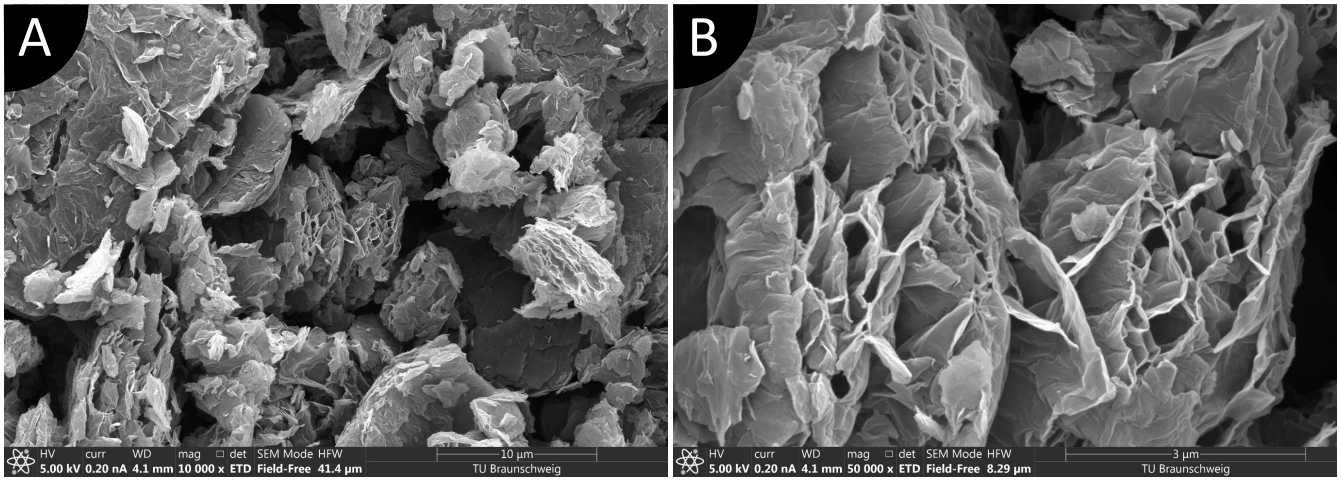

Fig. S6. SEM images of GO3: (A) ($\times 10,000$); (B) ($\times 50,000$).

MWCNTs used in this study show similarities to the morphology of MWCNTs reported in literature [17]. In contrast to hair-like MWCNTs, GNPs seem to have particle-like geometry and form huge agglomerations of diameters up to 50 μm, but

without the flaky structure which is known for GNPs from literature [18, 19]. As reported in literature [20], the morphology of GNP can vary greatly, and thus lead to different composite properties for the same GNPs content. Some researchers classified GNPs by lamellar, fragmented, and bulk [20]. From the SEM images (Fig S4), the GNPs used in this study are considered fragmented, and quite high loadings of this type of GNPs are necessary to improve composite properties. On the other hand, both GO materials used in this study look lamellar, consisting of multiple creased thin layers stacked together, similar to reports in literature [21]. Comparing GO2 and GO3 used in this study, GO3 takes twice as high volume for the same amount of GO2 because of almost twice as high surface area. As a result of different conductive nanofiller sizes/geometries/types used for composite manufacturing, different characteristics (cure depth, dielectric, mechanical, and piezoelectric properties) for every material composition are expected.

C. Suspension preparation

All suspensions prepared in this study are dispersed with the same method and parameters: two-step particle dispersion with ultrasonic sonotrode followed by solvent (ethanol (EtOH)) evaporation to form a paste (Fig S7 and S8).

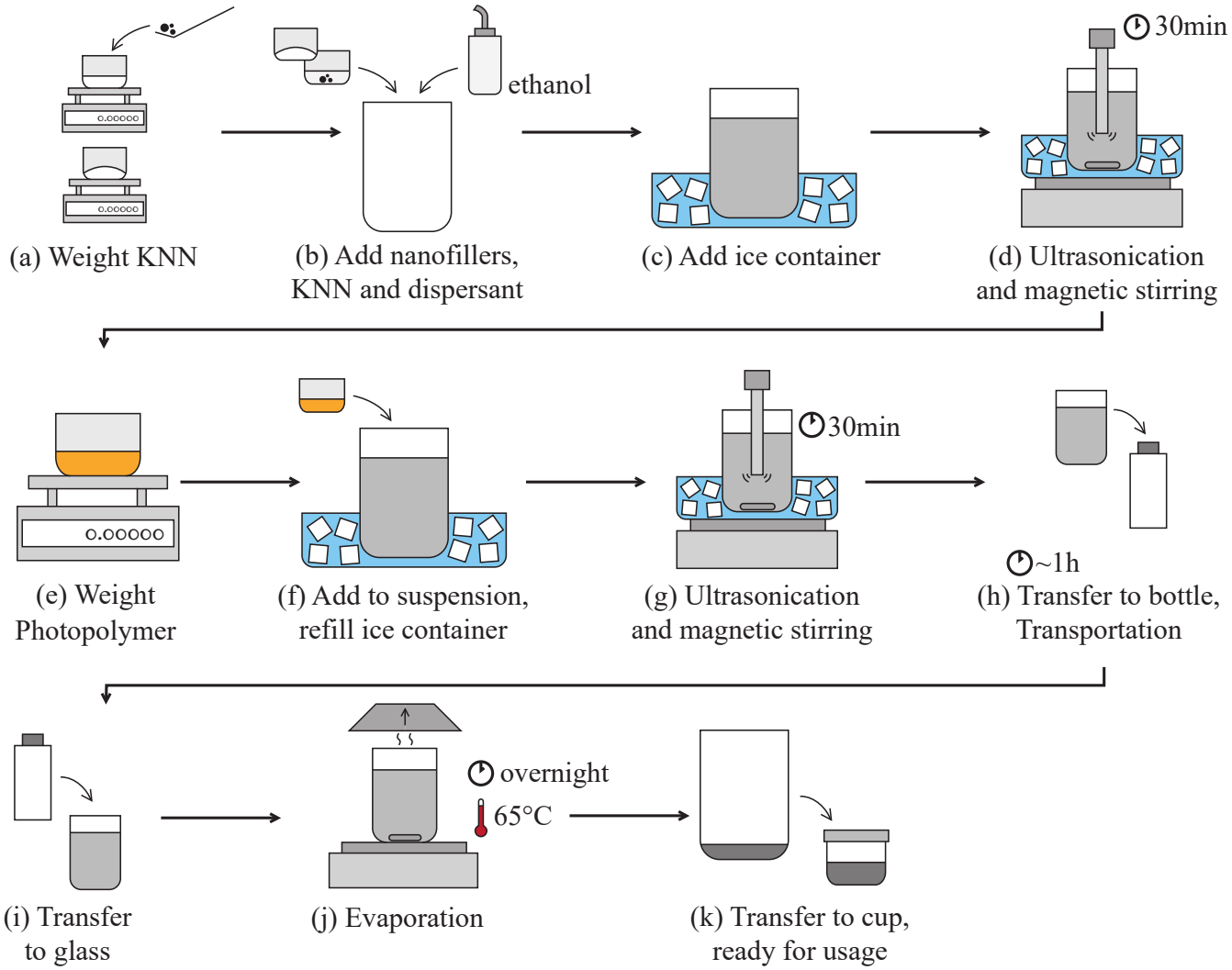

Fig. S7. Schematics of UV-light curable suspension preparation.

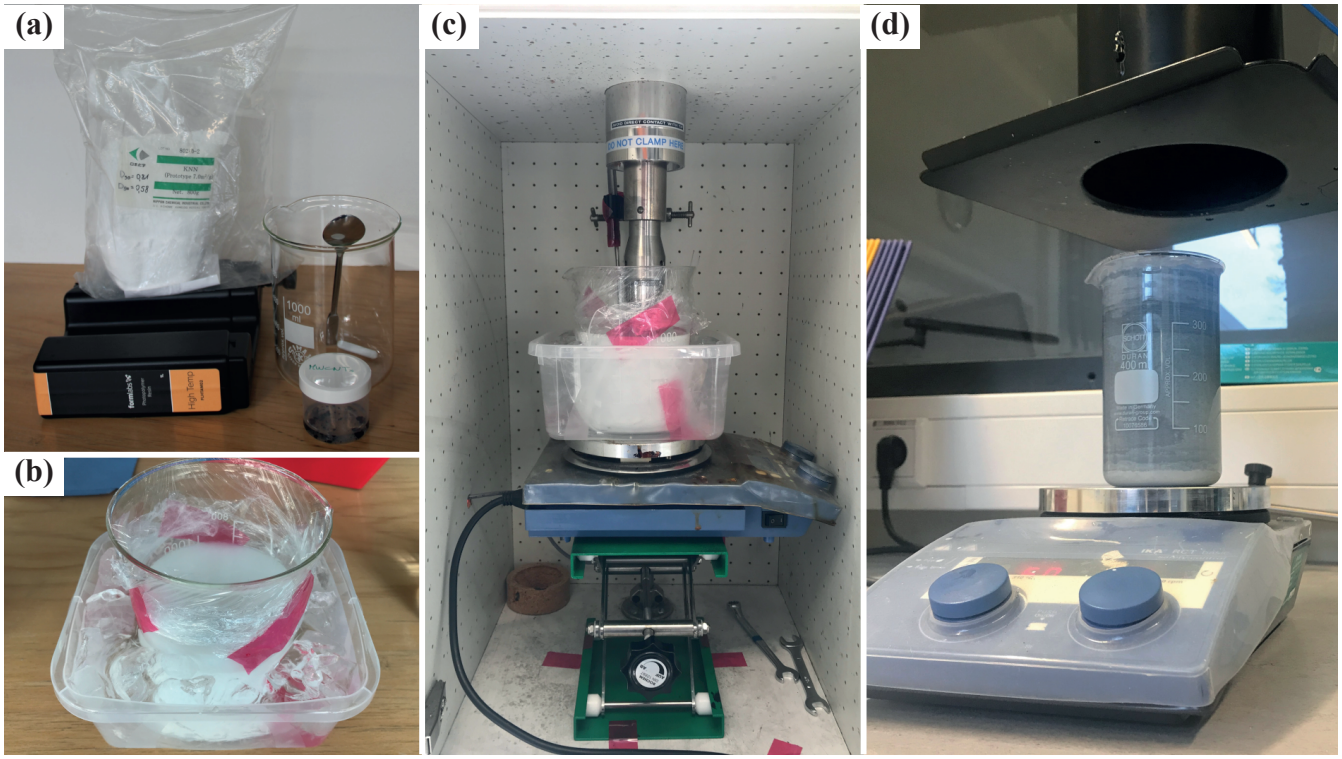

Fig. S8. Process of UV light curable suspension preparation: (A) Materials used; (B) Materials in a glass jar before ultrasonication; (C) Ultrasonication of materials with ultrasonic sonotrode; (D) Ethanol evaporation while gently heating and stirring.

In the first step, nanofiller and piezoelectric ceramic powder are added to ethanol. The amount of ethanol is determined to form either 5 wt.% ceramic/solvent or 2 wt.% nanofiller/solvent, whichever requires more ethanol. The glass jar is covered with plastic film (cling film) to avoid contamination, material splashing, and to minimize solvent evaporation during ultrasonication. The glass jar with the materials is placed in a plastic box, fixed to the bottom of the box, and water with crushed ice is filled around the glass jar to cool the suspension during ultrasonication (Fig S8 (B)). The suspension is ultrasonicated with ultrasonic sonotrode (Branson Ultrasonics™ S-250D Model Sonifier™ Digital Cell Disrupter, BRANSON Ultrasonics Corporation, Danbury, Connecticut, USA) for 30 minutes with maximum power set to 70% of 200 W and 1-sec ultrasonication, 0.2-sec pause intervals (Fig S8 (C)). Pauses are not taken into ultrasonication time. The actual power of ultrasonication varies depending on the viscosity of the material being ultrasonicated, which varies with the temperature. During ultrasonication, the actual ultrasonication power that affects the dispersion varies between 30-60 W and the temperature of dispersion varies between $8°C$ to $35°C$. The ultrasonic sonotrode and temperature sensor are immersed in the liquid through the small holes in the plastic foil. After the first ultrasonication step (30 minutes), a photopolymer is added, the glass jar is sealed again, crushed ice with water is added around the glass jar and the ultrasonication process is run for the next 30 min. After transportation of the dispersion to another facility, the dispersion is left overnight for solvent evaporation while stirring with an average-size magnet at 300 rpm and heating the dispersion to $65°C$, until all ethanol evaporates (Fig S8 (D)). The gentle heating of the dispersion during solvent evaporation produces a single-color suspension without clearly visible particles in the suspension or on the glass jar walls, opposite to cold evaporation. It is important to mention that all composites with BTO ceramics left some particles on the glass jar sides after evaporation, which were washed with ethanol after evaporation, and evaporation was continued until no ethanol was present in the suspensions.

D. Composite manufacturing and poling

Composite suspensions are solidified (cured) under UV light after tape-casting them manually on the glass (Fig S9). PVC film (Oracal 751C, thickness 60 μm), with three cut square geometries (20 x 20 mm), is glued on the glass (Fig S10 (A)). To decrease the adhesion between solidified composite and glass/sticker, a mold release agent (Safelease 30, AIRTECH Europe GmbH, Germany) was applied to the glass and sticker with a sponge as a single, thin layer and was dried at room temperature for a few minutes with a simple cooling fan. It helps to achieve higher solidified composite quality and reduces residual stresses in the composite.

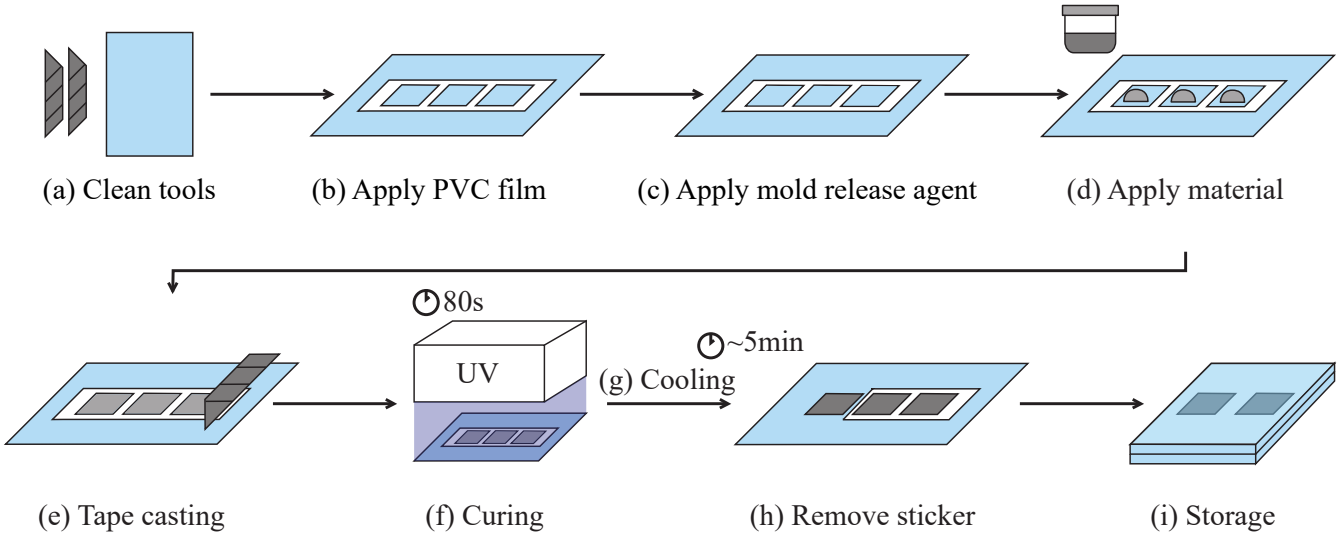

Fig. S9. Schematic representation of piezoelectric composite sensor forming and solidification.

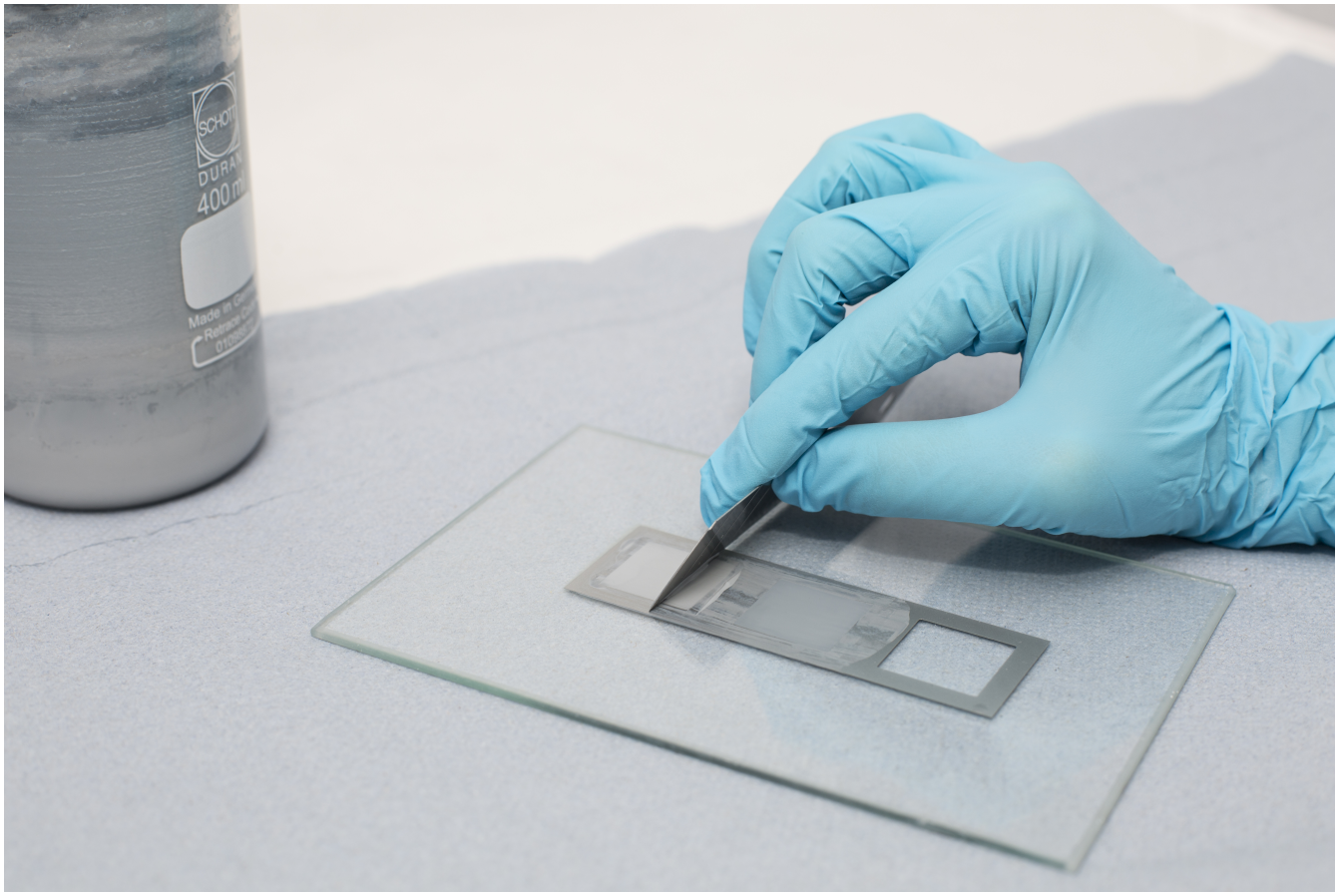

Fig. S10. Tape-casting of piezoelectric composite sensors

Afterward, the suspension is poured into the cut geometries and is tape-casted with a handheld metal blade at around 30°. The glass with a tape-cast composite suspension (together with PVC film) is placed 50 *mm* below the UV light source (EQ CL30 LED Flood, Henkel AG & Co. KGaA, Düsseldorf, Germany) for 80 seconds. UV light was applied only from a single side for all composites. The only exception is the curing cycle for six selected composites for further investigation (Young's modulus and piezoelectric measurements), where UV light was applied for 40 seconds from one side and after short cooling was applied for 40 seconds from another side to achieve higher homogeneity of the solidified composites. UV light source, with 405 *nm* wavelength,

produces 1.5 W/cm^2 at 50 mm distance. After composite solidification, the PVC foil is peeled off leaving solidified specimens on the glass (Fig S10 (F)). Peeled composites are washed with acetone and are kept between two glasses for a few days in the dark at room temperature to reduce bending (residual stresses). No additional post-curing with UV light or heat was applied.

After a selection of six composite materials for measurements of piezoelectric properties, a thin, single layer of conductive silver ink (Silberleitlack, type 530042, Ferro GmbH, Remchingen, Germany) is manually applied on both sides of the specimens, leaving 1 mm around the edges uncovered. Electrodes are required for dielectric measurements, poling, and piezoelectric properties measurements. The poling of the specimens took place in Silica oil heated to 55°C for in total of 21 minutes (4-minute ramp time, 16-minute hold time, 1-minute ramp-down time). All specimens were poled in a 30 kV/mm electric field.

E. Characterization methods

XRD patterns of ceramic materials were determined using Cu Kα radiation (Empyrean Cu LEF HR goniometer, Almelo, Netherlands) on a Si sample holder. XRD helps to determine if the ceramic powders used in this study are indeed piezoelectric, i.e. if materials have a non-cubic crystal lattice structure. XRD patterns were measured in the $10 - 90^\circ$ 2θ range in 0.05° steps, each step measured for 2 seconds at room temperature (Empyrean series 2, PANalytical PIXcel-3D detector, Almelo, Netherlands).

The curing depths of the suspensions are measured over time, using four curing times: 20, 40, 60, and 80 seconds. The specially designed, pre-cut PVC film with cut 8 mm size circles is glued on the glass [**?**], covering the whole glass, so that UV light can penetrate only through the holes. Specific holes are covered with a mask over time, creating different exposure times. The suspension being investigated is applied on the other side of the glass. Glass thickness is 1 mm. The glass plate with PVC film on the top side and suspension on the bottom side is placed under UV light at a distance of 50 mm. Sides are covered so that no UV light exposure would occur from other directions. After applying UV light for 20 seconds, the first mask is applied, covering a few holes, and the UV light is applied for further 20 seconds. The process is repeated until the final curing time (80 seconds) for the last holes is reached. Not solidified material is removed manually and the solidified composite material on the glass is cleaned with isopropyl alcohol. After the removal of solidified circles from the glass, the thickness of cured circles is measured with a micrometer with up to 2 μm accuracy to measure curing depth.

SEM is used to investigate as-received ceramic particles, nanofillers, and the cross-sections of broken, solidified piezoelectric composite sensors. Helios G4 CX DualBeam™ SEM imaging system (Thermo Fisher Scientific, Waltham, US) was used. Ceramic particles and nanofillers were applied to the conductive sticky tape without any force. Solidified composite sensors were broken at room temperature to investigate their cross-sections. All specimens for SEM (particles, nanomaterials, and cross-sections of the solidified composites) were sputtered with a 4 nm thickness platinum layer before scanning to achieve a higher contrast.

Dielectric measurements in this study include measurements of relative permittivity ϵ_r and dielectric loss (dissipation factor $tan(\delta)$) at 1 kHz at room temperature. For dielectric measurements, at least 5 specimens of every composition were measured. Two types of dielectric measurements were made: without electrodes on the piezoelectric composites and with electrodes. The first method (without electrodes) was used to measure the dielectric properties of all composites manufactured in this study to roughly compare their dielectric properties. Because no electrodes were applied, the sensors were sandwiched between a bigger copper plate and a smaller stainless steel plate to keep the measurement area constant between measurements. The principle of measurement is shown in Fig S11. In this way, piezoelectric composite sensor dielectric properties can be compared between materials without electrodes. Unfortunately, using this method the dielectric properties are not comparable to other studies.

Fig. S11. Principle of measurement of dielectric properties without applied electrodes.

After the manufacturing of all planned material compositions, the specimens of six selected compositions were covered with silver electrodes (described above) and their dielectric properties were remeasured. The dielectric properties of these six selected composites can be compared to the literature. The relative permittivity is calculated by measuring the capacitance of specimens at 1 kHz with an LCR meter (LCR-300, Voltrcraft, Conrad Electronic SE, Hirschau, Germany. Basic accuracy 0.3% with 0.01% resolution) using Eq. (1):

$$\epsilon_r = \frac{C \times d}{\epsilon_0 \times A} \tag{S1}$$

where C — capacitance of the specimen at a respective frequency (F), d — average thickness of the specimen (m), ϵ_0 — permittivity of a vacuum, constant ($8.84 \times 10^{-12}\ F/m$), A — overlapping electrode area of the specimen (m^2). The dielectric losses are directly measured by the LCR meter.

Young's modulus of the piezoelectric composites was measured for piezoelectric charge coefficient determination with a tensile testing machine (Zwick Roell Z1.0, ZwickRoell GmbH & Co. KG, Ulm, Germany). Because of the manufacturing limitations, 30 x 20 mm specimens, with thickness varying between 0.055 mm and 0.12 mm, were prepared for tensile testing (all manufactured as a single layer). At least ten specimens per investigated material composition (without electrodes and not poled) were tested at least 48 hours after specimen manufacturing. Special grippers for thin foils were used to ensure about 7 mm grip area on both ends of the specimens. Because of the nature of foils, a pretension of 2 N was applied at a speed of 1 mm/min. Tensile testing was also done at a speed of 1 mm/min at room temperature. Because of the small specimen size, no extensometer or visual strain measuring methods were available. Therefore, the force and displacement measured by the machine were used to approximate Young's modulus. Young's modulus was determined as an approximation from Eq. (2):

$$E = \frac{\sigma_2 - \sigma_1}{\varepsilon_2 - \varepsilon_1} \tag{S2}$$

where σ_1 — assumed normal stress (Pa) at $\varepsilon_1 = 0.0005$ and σ_2 — assumed normal stress (Pa) at $\varepsilon_2 = 0.0025$ according to DIN EN ISO 527-1:2019.

To characterize and compare the performance of the sensors manufactured in this study, piezoelectric charge coefficients d_{31} were measured. Because of the thin, flexible specimen nature and polymer matrix used, most piezoelectric charge coefficient measuring methods, especially the ones that apply single-point loading, cannot be used or would produce wrong results. Digital Image Correlation (DIC) measurements are also problematic because of the high voltages needed to actuate the piezoelectric

composite materials and their small deformations. Therefore, we adapted the method developed by Payo [22] and slightly modified it. The method of piezoelectric charge coefficient d_{31} measurement is described in detail in our previous publication [23]. It is extremely important to mention that the piezoelectric properties reported in this study are effective piezoelectric properties because the sensors were characterized while glued on the substrate. Literature suggests, that in such a setup, measured piezoelectric values are approx. 40% lower than by using measuring methods using free-clamped samples [24].

In a 4-point bending test, a thin beam of glass-fiber reinforced plastic was excited harmonically (sinusoidally) below the first natural frequency at 30 Hz at room temperature, with two strain gauge sensors and piezoelectric composite sensors glued on it. This measuring approach works up to the first resonance frequency of the beam (<45 Hz) and can be used for d_{31} measurements at low frequencies. Two single-direction strain gauges were glued on both sides of the beam to form a half-bridge configuration for the temperature compensation and to measure strains on the surface of the beam. In total four piezoelectric composite sensors at the time (two on one side, two on another) were glued on the beam, their generated charge during harmonic loading was amplified with charge amplifiers (Kistler type 5001, Kistler Instrumente GmbH, Sindelfingen, Germany) and all data were recorded with HBM QuantumX MX440B module (Hottinger Brüel Kjaer GmbH, Darmstadt, Germany). All data were further processed with Matlab, to filter 50 Hz from the measured signal (additional noise from the power outlet), to apply a low-pass filter (<250 Hz) on the measured data (noise reduction), and to calculate piezoelectric charge coefficients d_{31}. For every material composition, at least 4 sensors were measured, harmonically exciting them for 15 seconds at least 10 times each, while 5 times exciting them when the piezoelectric composite sensors on the beam face upward, and 5 times when the beam is flipped and sensors face downward. All sensors were glued with fast-acting thin cyanoacrylate adhesives. For more details regarding piezoelectric charge coefficient d_{31} measurement the reader is referenced to our previous publication [23]. To wire piezoelectric composite sensors for measurement, before gluing them on the beam, the corner of the electrode on one side of the specimen was cleaned with acetone, and a connection through the specimen corner to the bottom electrode was made with the same conductive silver ink used to make electrodes in the first place. With this approach, the full surface of the sensor is glued flush on the beam while cables required to connect both electrodes can be glued from the same side.

By knowing the strain experienced on the surface of the beam and the electric charge produced by the piezoelectric composite sensors, d_{31} was calculated with Eq. (3):

$$d_{31} = \frac{1 - v}{E} \times S \tag{S3}$$

where v – Poisson's ratio, E – Young's modulus (Pa), and S – sensitivity ($(C/m^2)/(m/m)$). Poisson's ratio value of 0.3 is selected because most polymers have Poisson's ratio between 0.25 and 0.35 [22]. The sensitivity of the piezoelectric composite sensors S is calculated with Eq. (4):

$$S = \frac{Q}{\varepsilon \times A} \tag{S4}$$

where Q – electric charge generated by piezoelectric sensor (C), ε - strain measured on the surface of the beam (m/m), and A – overlapping electrode area of the piezoelectric sensor (m^2).

Piezoelectric voltage coefficient g_{31} was calculated from d_{31} using Eq. (5):

$$g_{31} = \frac{d_{31}}{\varepsilon_0 \times \varepsilon_r} \tag{S5}$$

where ε_0 - constant, permittivity of vacuum (F/m), and ε_r - relative permittivity, at room temperature, at 1 kHz (-).

2. RESULTS. SEM OF COMPOSITES

A. Composites without nanofillers

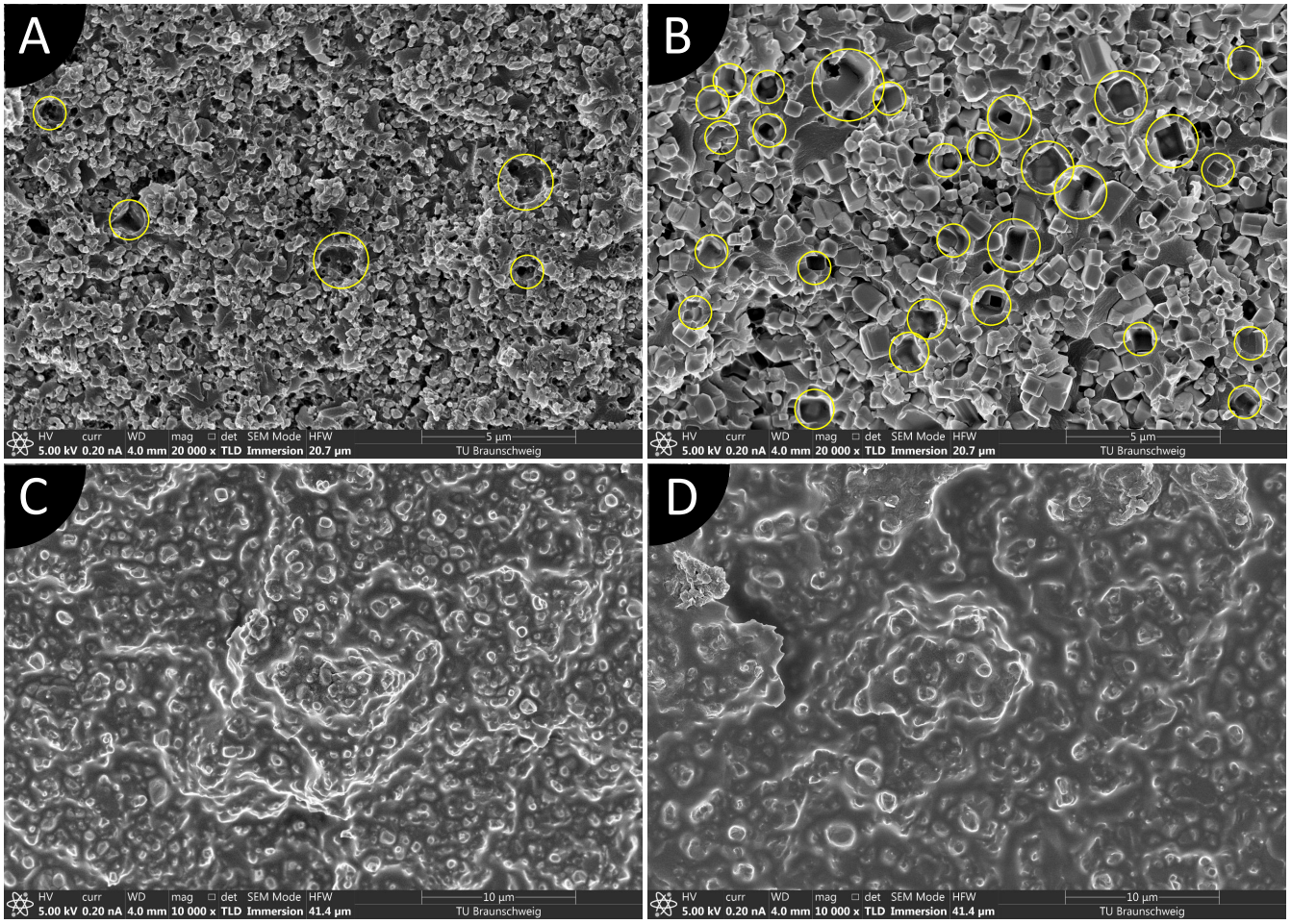

Fig. S12. SEM image of (A) 30KNN3 ($\times 20,000$), (B) 30KNN6 ($\times 20,000$), (C) 30BTO7 ($\times 10,000$), (D) 30BTO13 ($\times 10,000$). Yellow circles show clearly visible missing particles.

B. Composites with GNPs

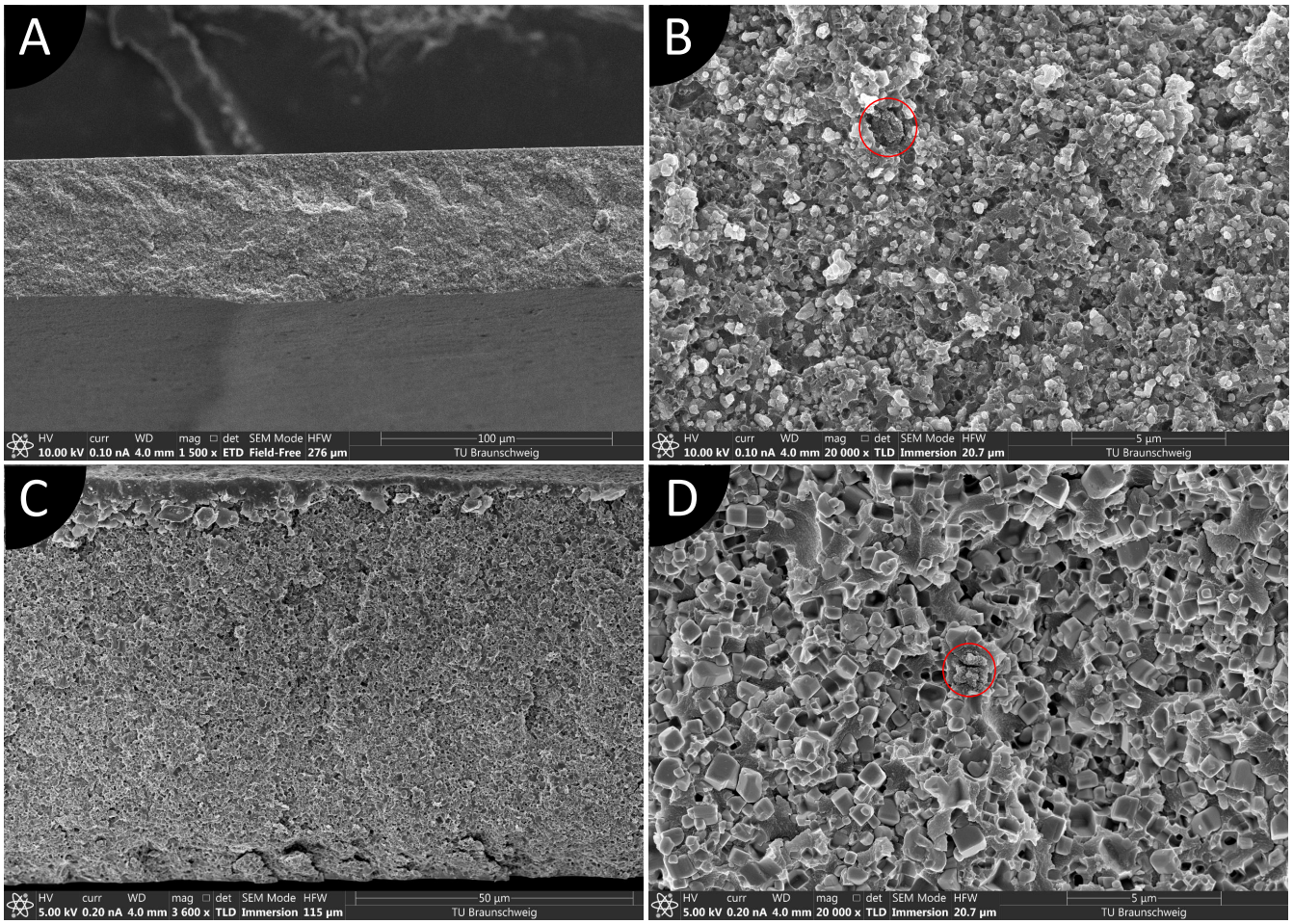

Fig. S13. SEM images of KNN composites with 0.2 wt.% GNPs: (A) 30KNN3-0.2GP ($\times 1,500$), (B) 30KNN3-0.2GP ($\times 20,000$), (C) 30KNN6-0.2GP ($\times 3,600$), (D) 30KNN6-0.2GP ($\times 20,000$). Red circles indicate GNPs where easily recognisable.

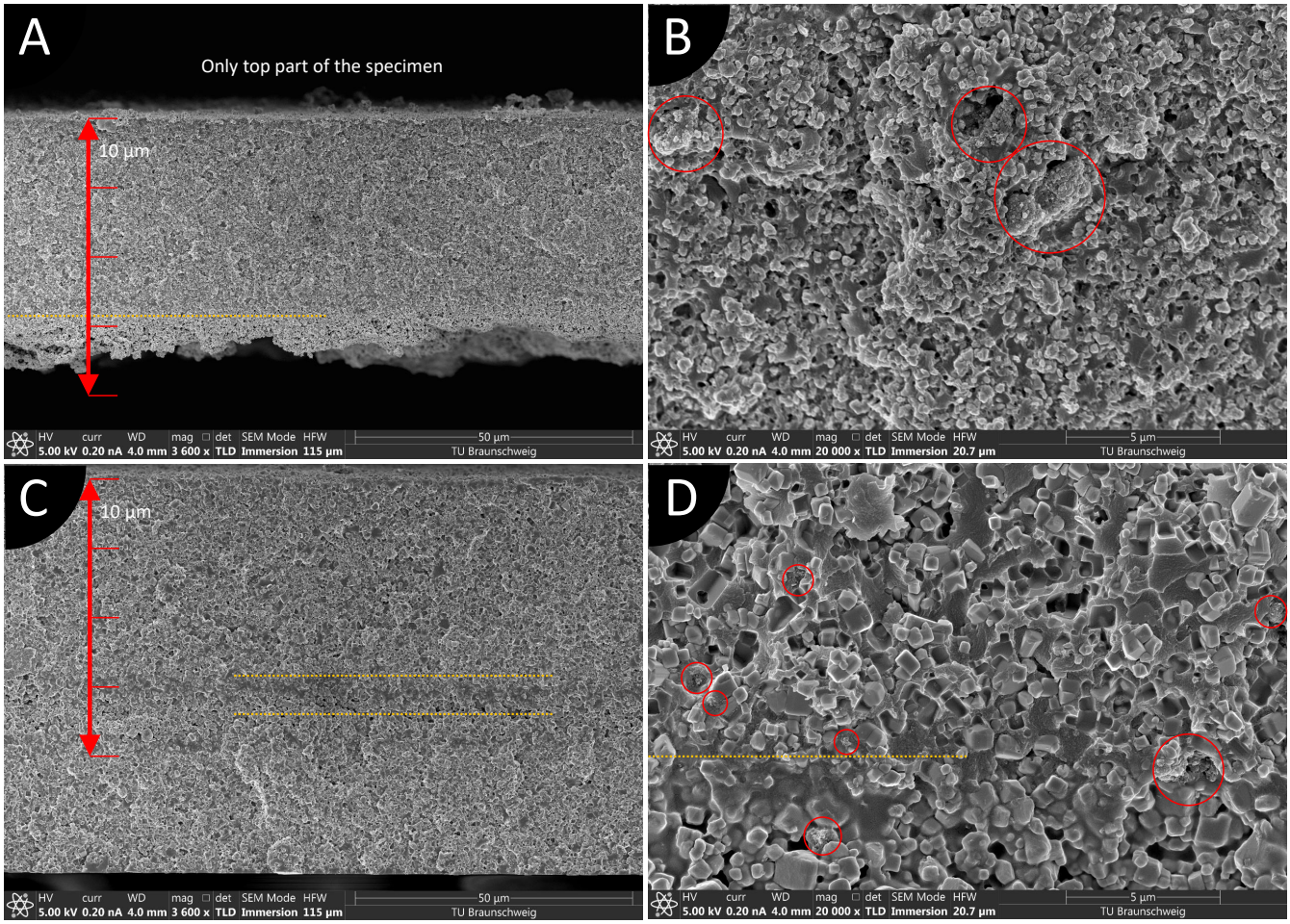

Fig. S14. SEM images of KNN composites with 0.4 wt.% GNPs: (A) 30KNN3-0.4GP ($\times 3,600$), (B) 30KNN3-0.4GP ($\times 20,000$), (C) 30KNN6-0.4GP ($\times 3,600$), (D) 30KNN6-0.4GP ($\times 20,000$). Orange dashed lines indicate change in photopolymer solidification degree. Red arrow shows depth of cure, gaps between markings are 10 μm. Red circles indicate GNPs where easily recognisable.

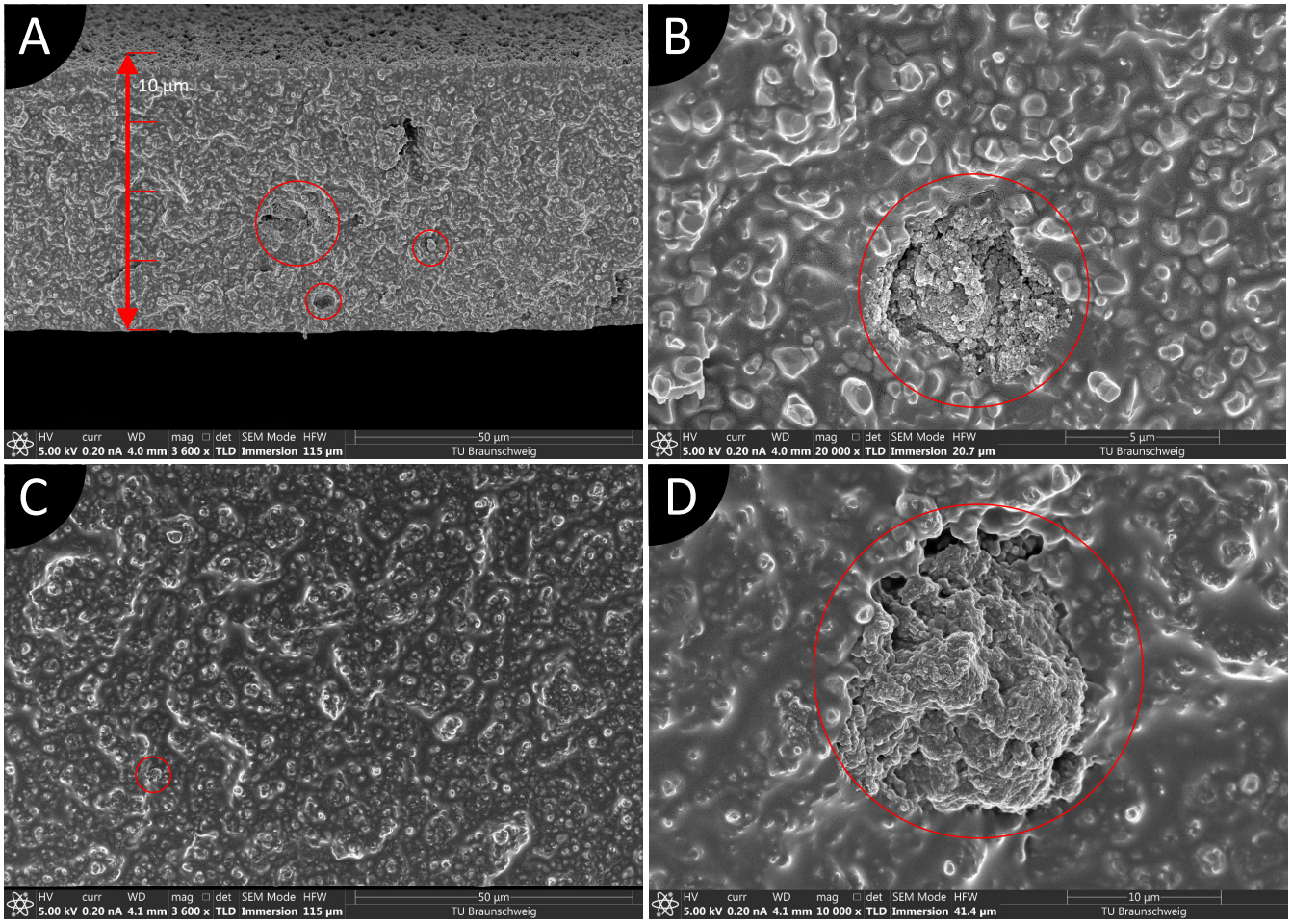

Fig. S15. SEM images of BTO composites with 0.2 wt.% GNPs: (A) 30BTO7-0.2GP ($\times 1,500$), (B) 30BTO7-0.2GP ($\times 20,000$), (C) 30BTO13-0.2GP ($\times 3,600$), (D) 30BTO13-0.2GP ($\times 10,000$). Red arrow shows depth of cure, gaps between markings are 10 μm. Red circles indicate GNPs where easily recognisable.

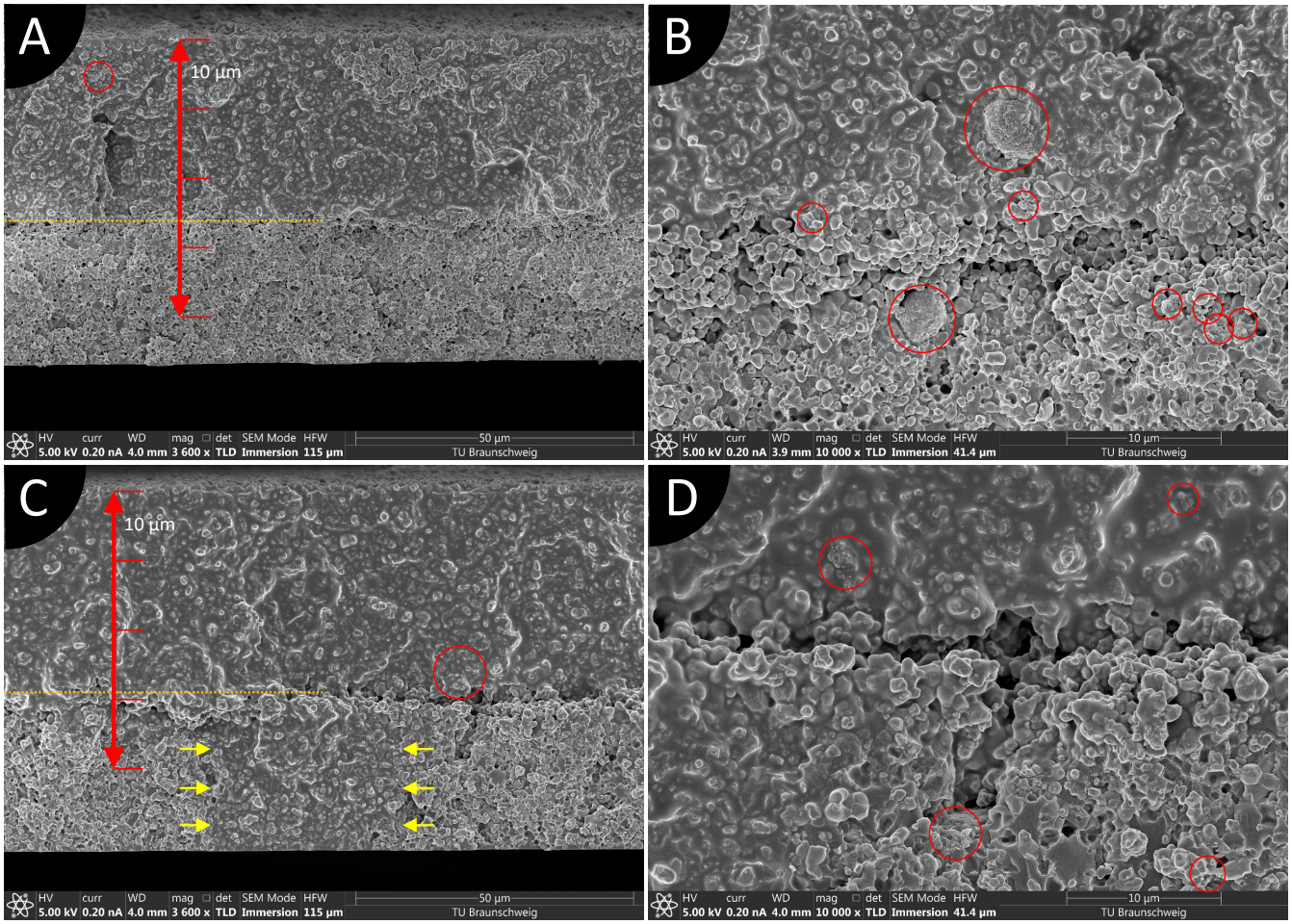

Fig. S16. SEM images of BTO composites with 0.4 wt.% GNPs: (A) 30BTO7-0.4GP ($\times 1,500$), (B) 30BTO7-0.4GP ($\times 20,000$), (C) 30BTO13-0.4GP ($\times 3,600$), (D) 30BTO13-0.4GP ($\times 10,000$). Orange dashed lines indicate change in photopolymer solidification degree. Red arrow shows depth of cure, gaps between markings are 10 μm. Red circles indicate GNPs where easily recognisable. Yellow arrows indicate different photopolymer degree of cure.

C. Composites with MWCNTs

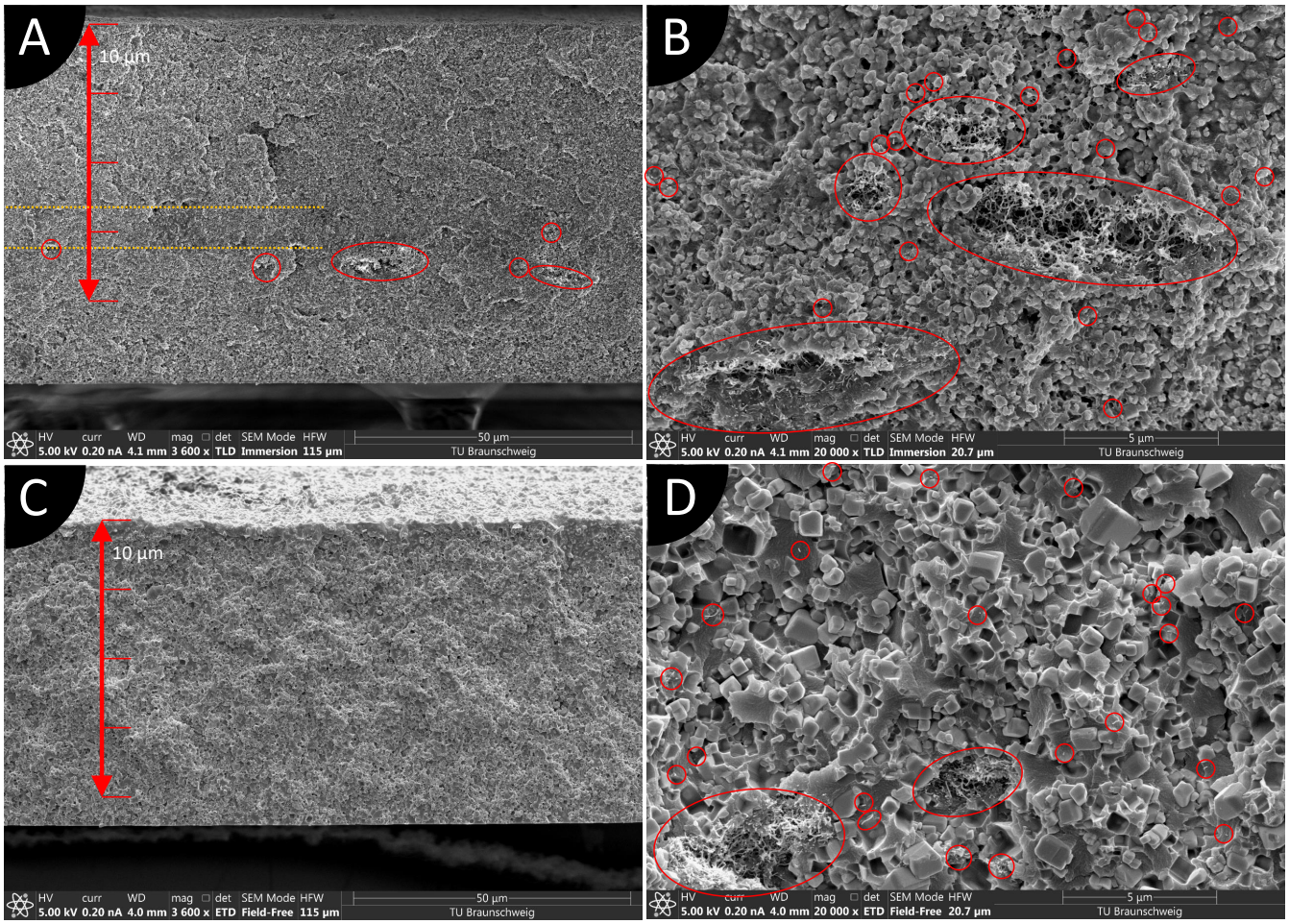

Fig. S17. SEM images of KNN composites with 0.2 wt.% MWCNTs: (A) 30KNN3-0.2M ($\times 3,600$), (B) 30KNN3-0.2M ($\times 20,000$), (C) 30KNN6-0.2M ($\times 3,600$), (D) 30KNN6-0.2M ($\times 20,000$). Orange dashed lines indicate change in photopolymer solidification degree. Red arrow shows depth of cure, gaps between markings are 10 μm. Red circles indicate MWCNTs where easily recognisable.

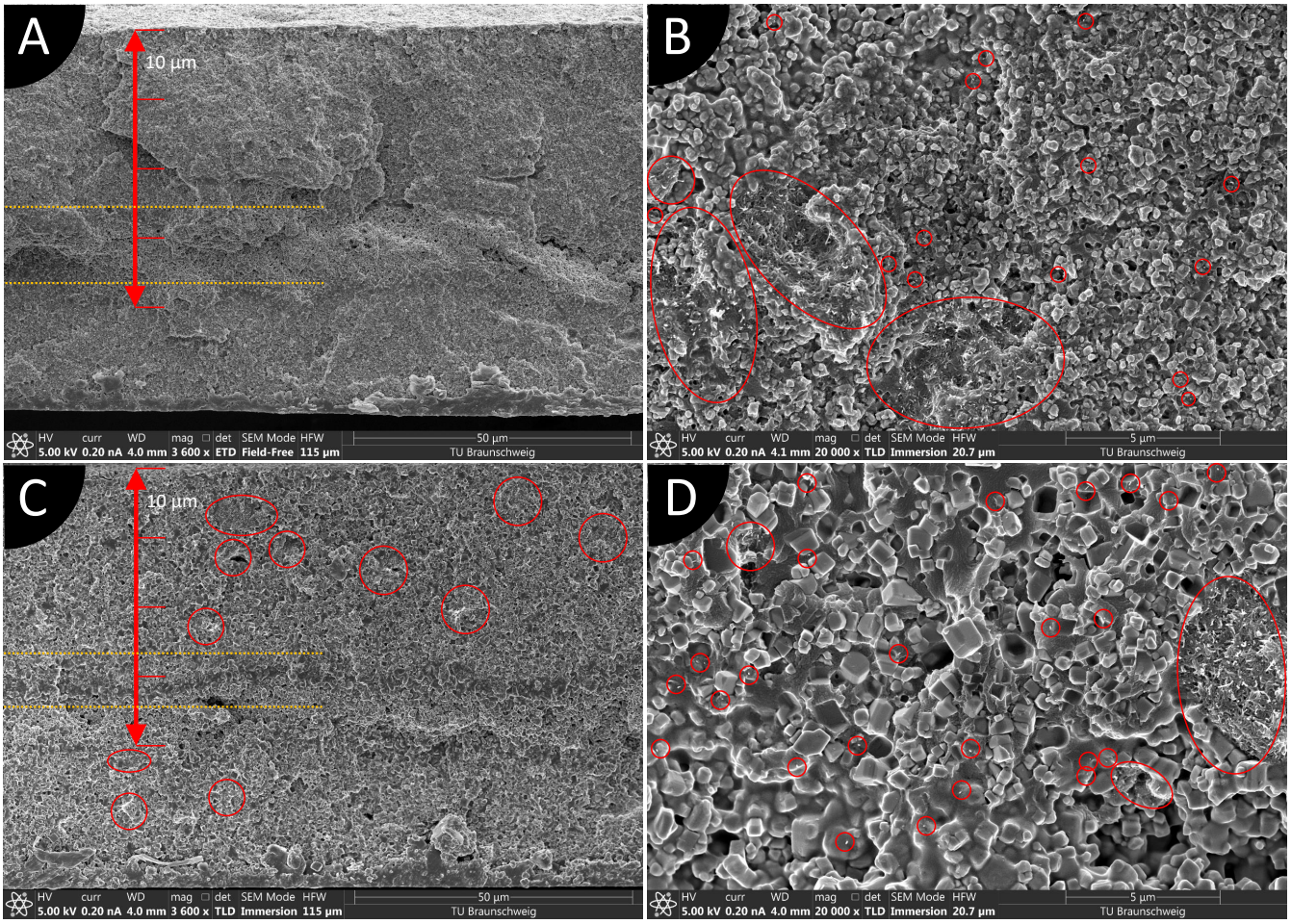

Fig. S18. SEM images of KNN composites with 0.4 wt.% MWCNTs: (A) 30KNN3-0.4M ($\times 3,600$), (B) 30KNN3-0.4M ($\times 20,000$), (C) 30KNN6-0.4M ($\times 3,600$), (D) 30KNN6-0.4M ($\times 20,000$). Orange dashed lines indicate change in photopolymer solidification degree. Red arrow shows depth of cure, gaps between markings are 10 μm. Red circles indicate MWCNTs where easily recognisable.

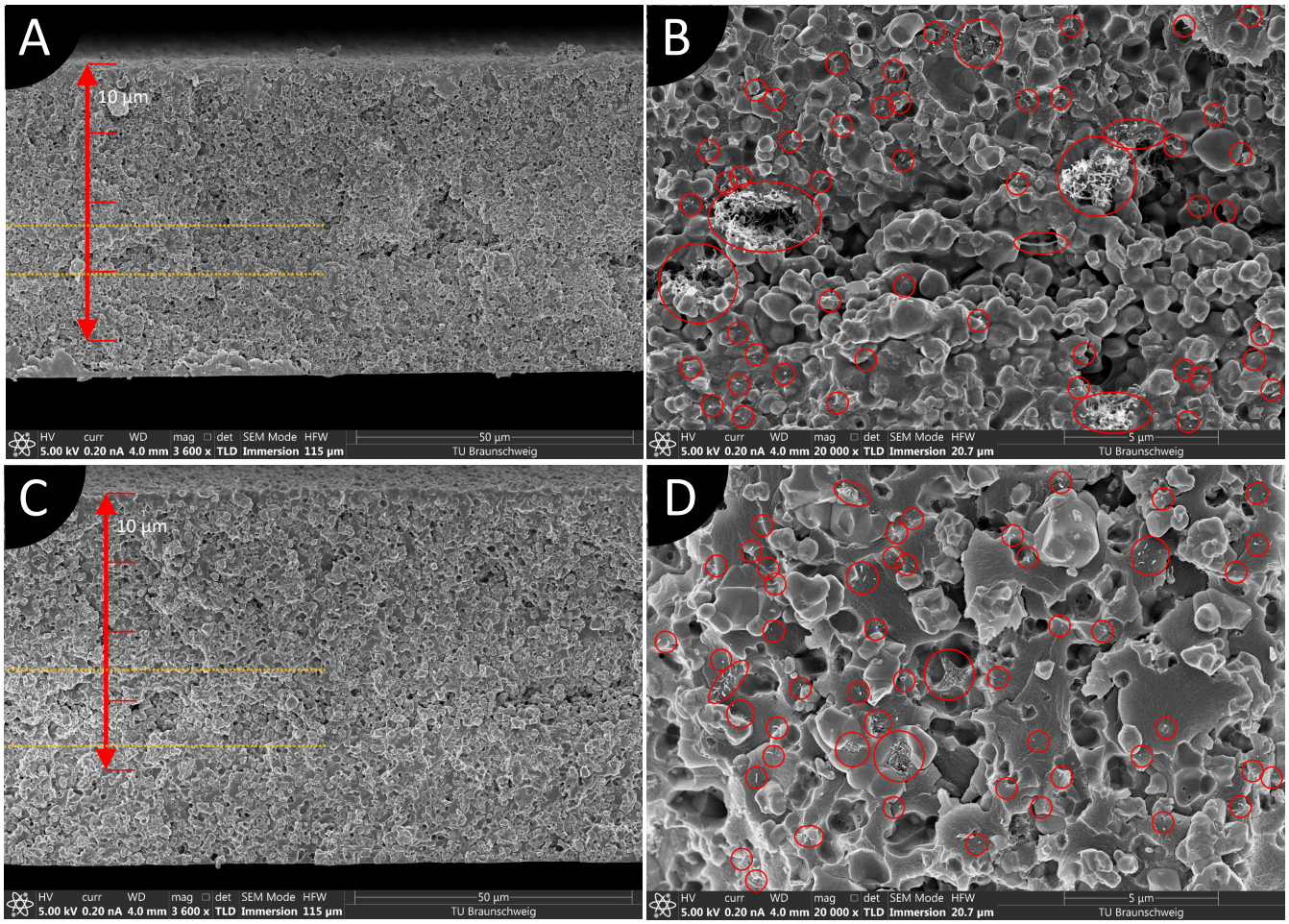

Fig. S19. SEM images of BTO composites with 0.2 wt.% MWCNTs: (A) 30BTO7-0.2M ($\times 3,600$), (B) 30BTO7-0.2M ($\times 20,000$), (C) 30BTO13-0.2M ($\times 3,600$), (D) 30BTO13-0.2M ($\times 20,000$). Orange dashed lines indicate change in photopolymer solidification degree. Red arrow shows depth of cure, gaps between markings are 10 μm. Red circles indicate MWCNTs where easily recognisable.

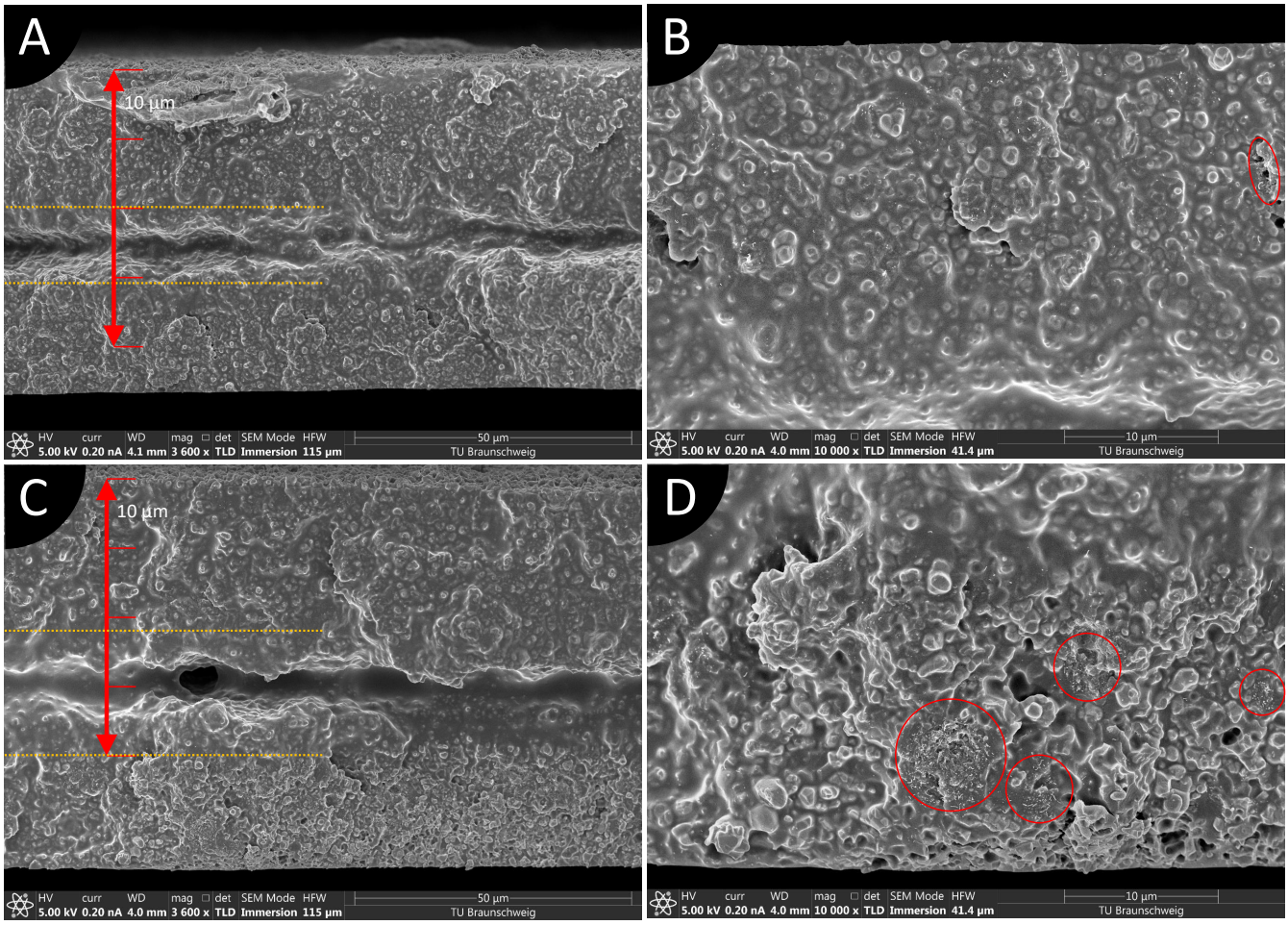

Fig. S20. SEM images of BTO composites with 0.4 wt.% MWCNTs: (A) 30BTO7-0.4M ($\times 3,600$), (B) 30BTO7-0.4M ($\times 10,000$), (C) 30BTO13-0.4M ($\times 3,600$), (D) 30BTO13-0.4M ($\times 10,000$). Orange dashed lines indicate change in photopolymer solidification degree. Red arrow shows depth of cure, gaps between markings are 10 μm. Red circles indicate MWCNTs where easily recognisable.

D. Composites with GO2

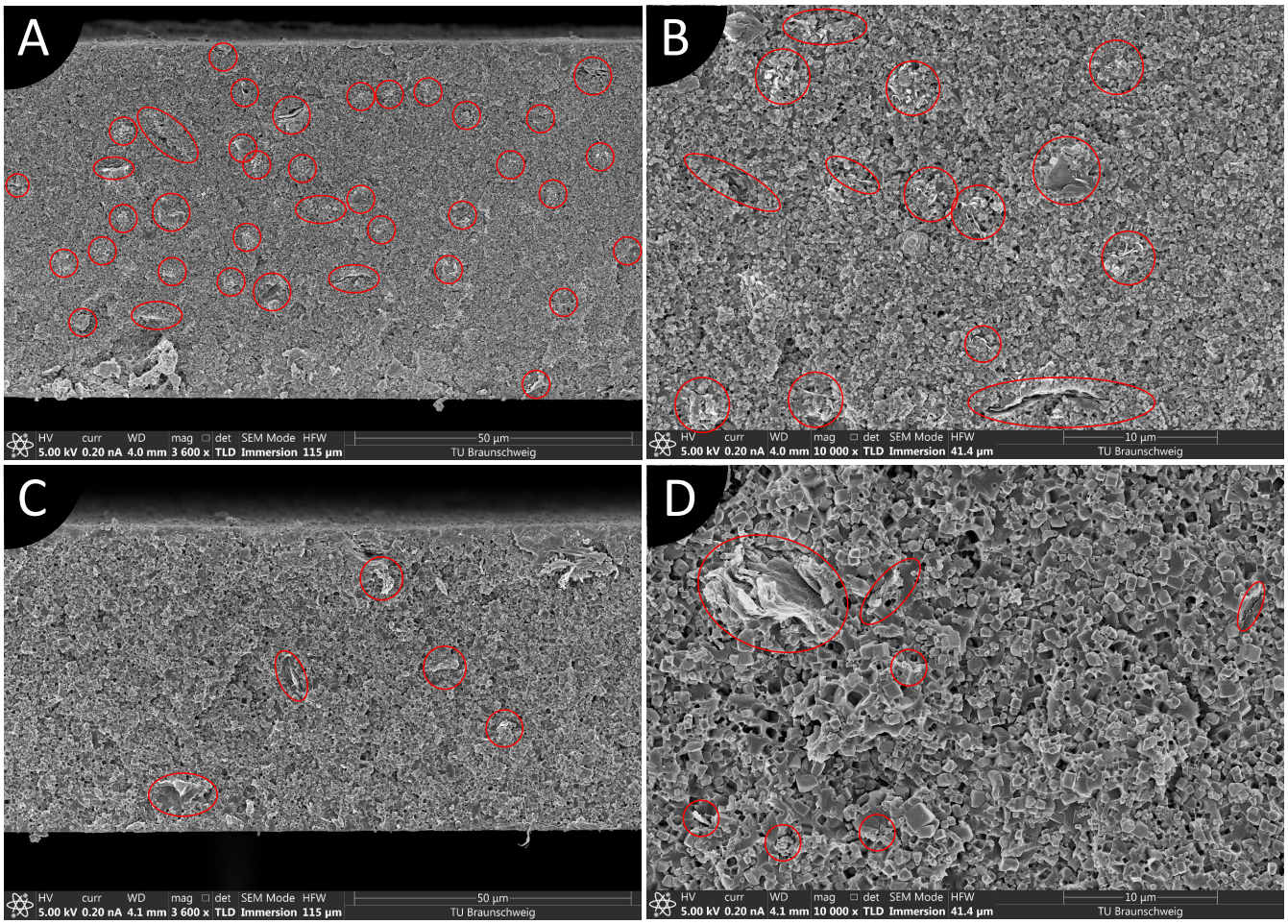

Fig. S21. SEM images of KNN composites with 0.2 wt.% GO2: (A) 30KNN3-0.2GO2 ($\times 3,600$), (B) 30KNN3-0.2GO2 ($\times 10,000$), (C) 30KNN6-0.2GO2 ($\times 3,600$), (D) 30KNN6-0.2GO2 ($\times 10,000$). Red circles indicate GO2 where easily recognisable.

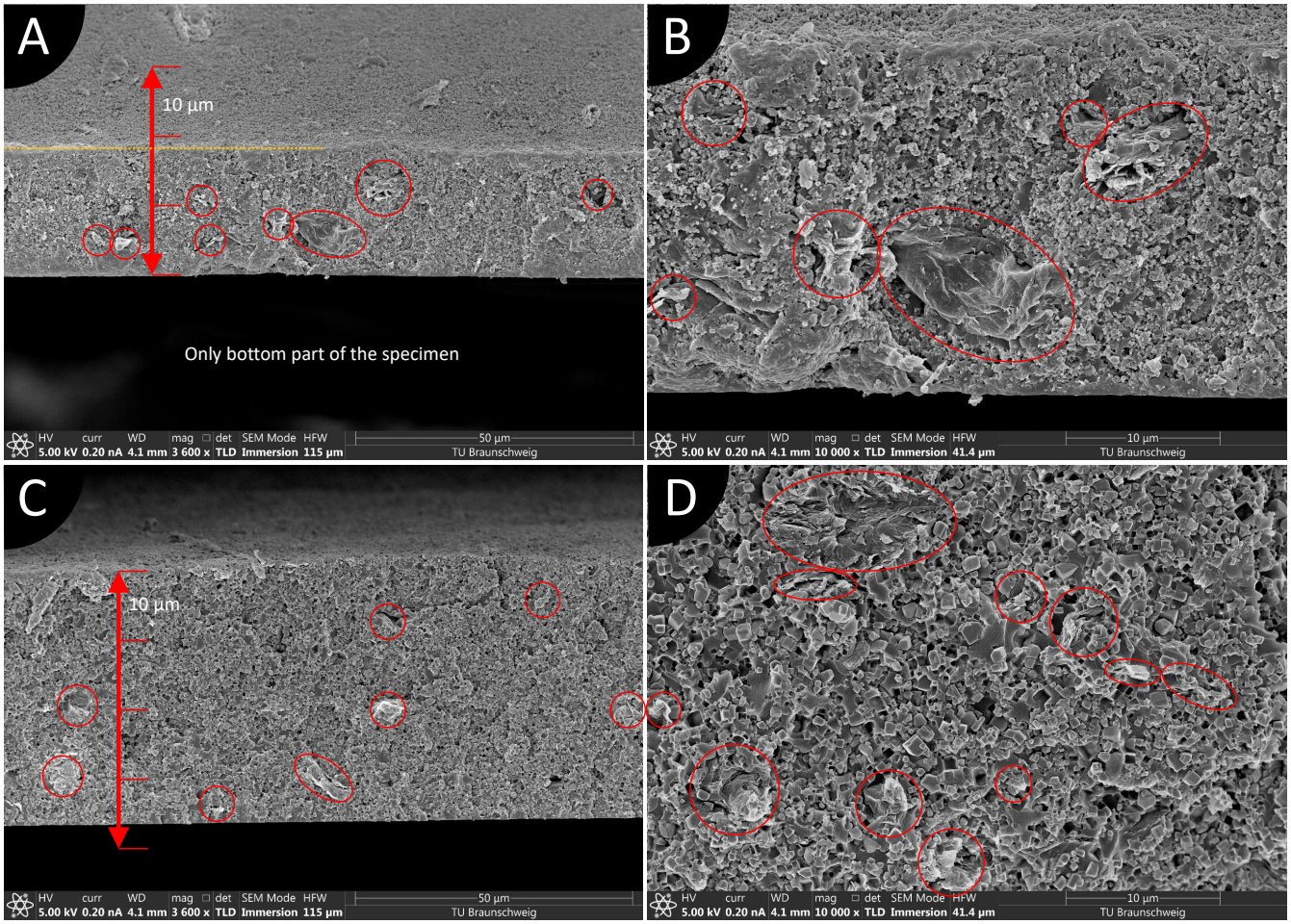

Fig. S22. SEM images of KNN composites with 0.4 wt.% GO2: (A) 30KNN3-0.4GO2 ($\times 3,600$), (B) 30KNN3-0.4GO2 ($\times 10,000$), (C) 30KNN6-0.4GO2 ($\times 3,600$), (D) 30KNN6-0.4GO2 ($\times 10,000$). Orange dashed lines indicate change in photopolymer solidification degree. Red arrow shows depth of cure, gaps between markings are 10 μm. Red circles indicate GO2 where easily recognisable.

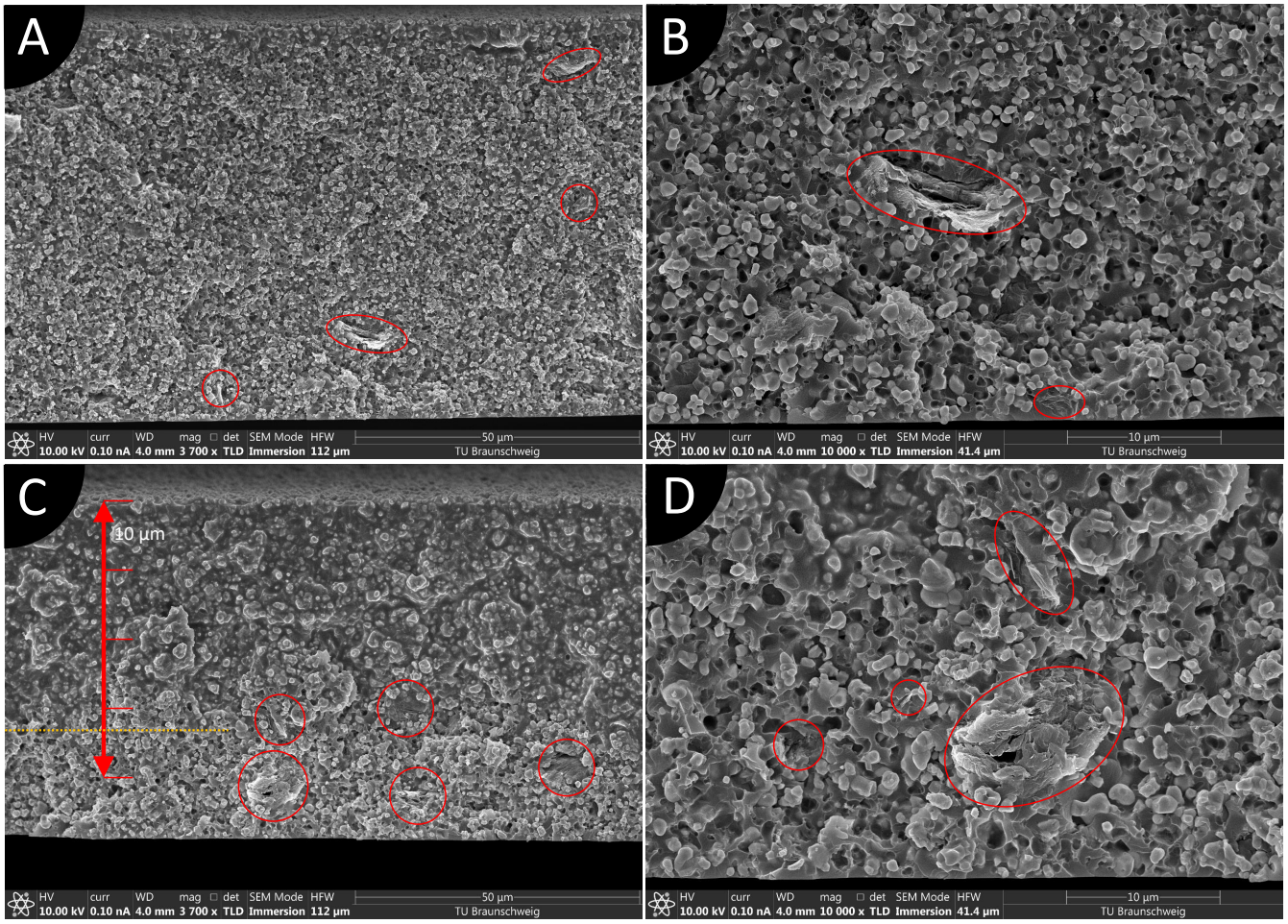

Fig. S23. SEM images of BTO composites with 0.2 wt.% GO2: (A) 30BTO7-0.2GO2 ($\times 3,700$), (B) 30BTO7-0.2GO2 ($\times 10,000$), (C) 30BTO13-0.2GO2 ($\times 3,700$), (D) 30BTO13-0.2GO2 ($\times 10,000$). Orange dashed lines indicate change in photopolymer solidification degree. Red arrow shows depth of cure, gaps between markings are 10 μm. Red circles indicate GO2 where easily recognisable.

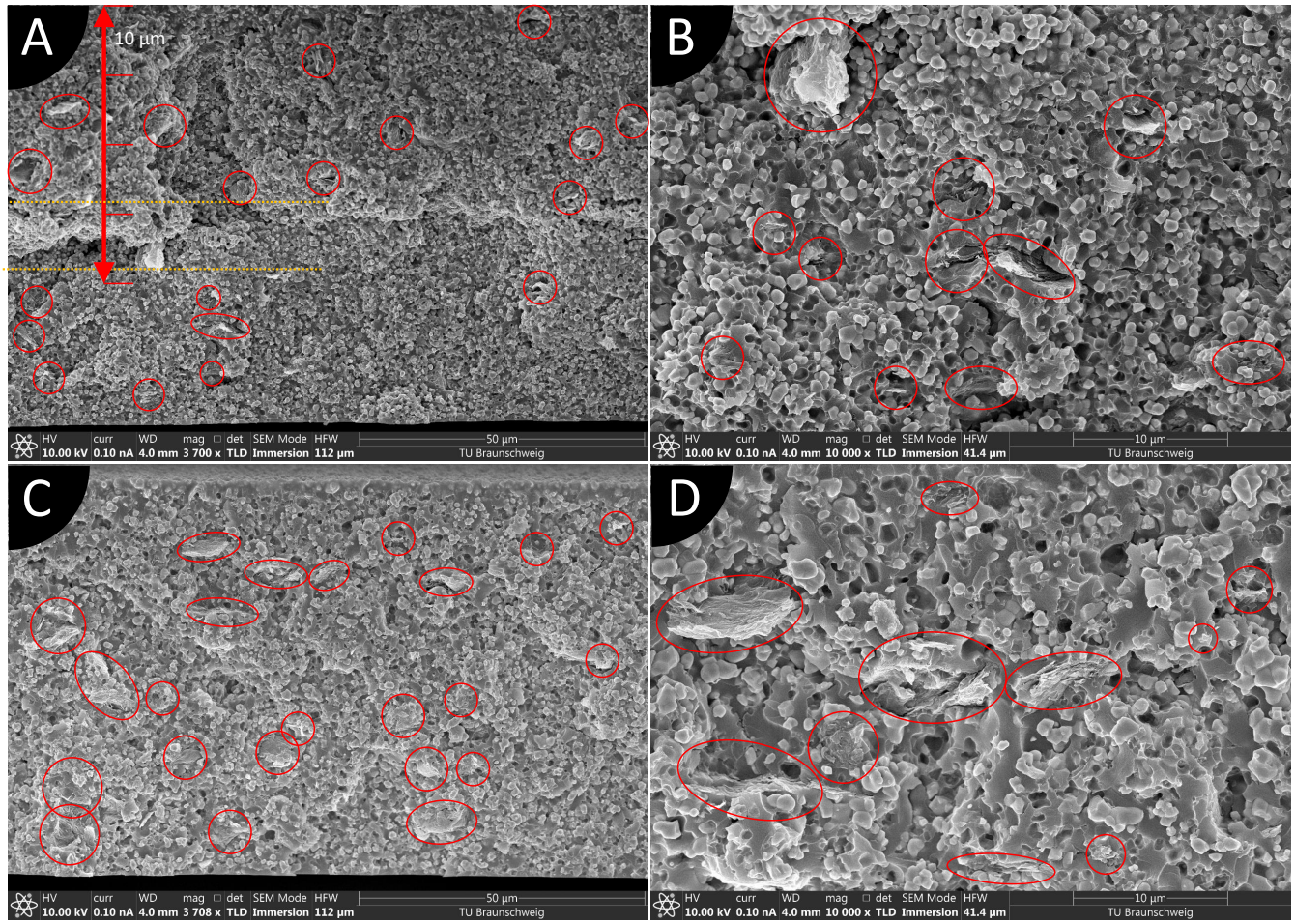

Fig. S24. SEM images of BTO composites with 0.4 wt.% GO2: (A) 30BTO7-0.4GO2 ($\times 3,700$), (B) 30BTO7-0.4GO2 ($\times 10,000$), (C) 30BTO13-0.4GO2 ($\times 3,700$), (D) 30BTO13-0.4GO2 ($\times 10,000$). Orange dashed lines indicate change in photopolymer solidification degree. Red arrow shows depth of cure, gaps between markings are 10 μm. Red circles indicate GO2 where easily recognisable.

E. Composites with GO3

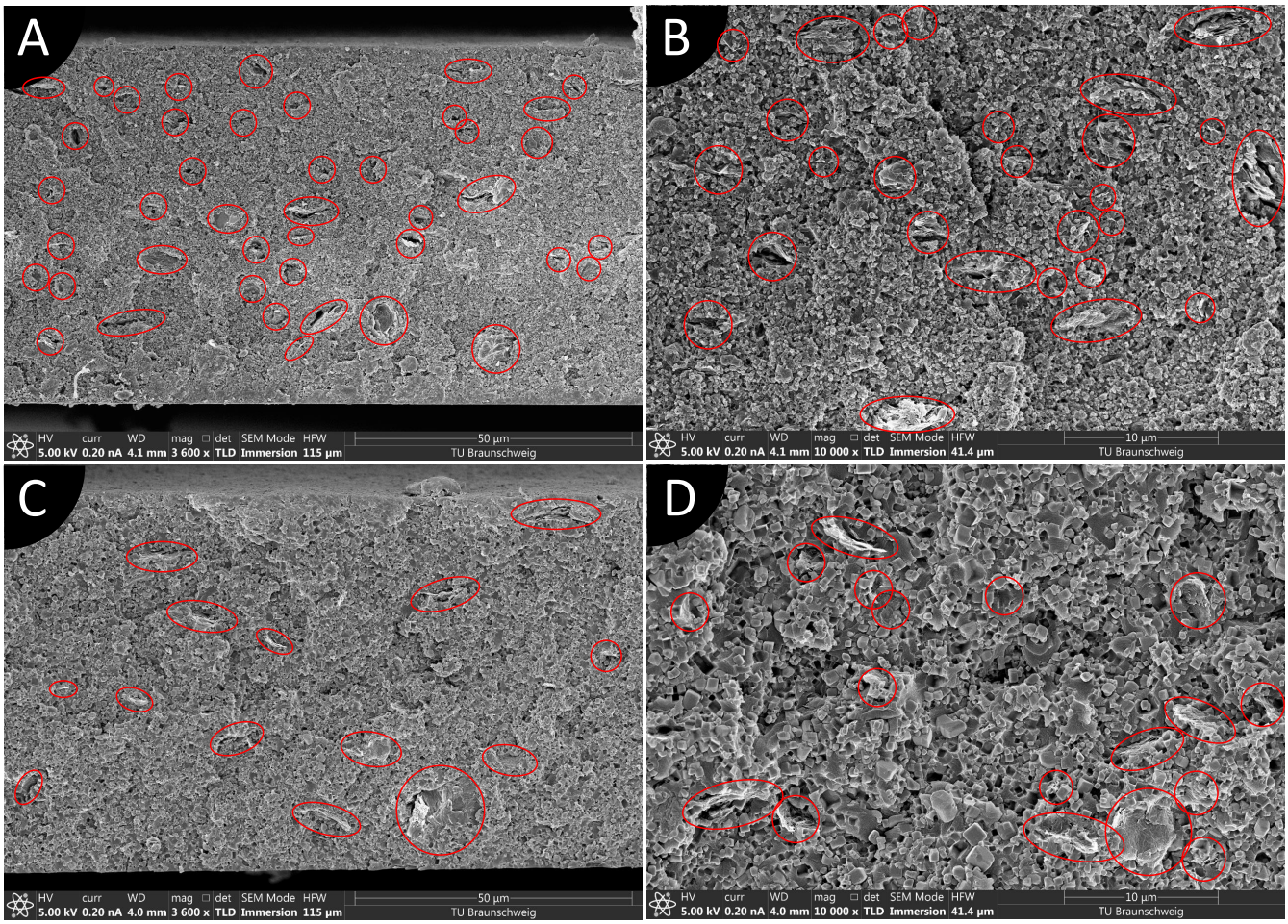

Fig. S25. SEM images of KNN composites with 0.2 wt.% GO3: (A) 30KNN3-0.2GO3 ($\times 3,600$), (B) 30KNN3-0.2GO3 ($\times 10,000$), (C) 30KNN6-0.2GO3 ($\times 3,600$), (D) 30KNN6-0.2GO3 ($\times 10,000$). Red circles indicate GO3 where easily recognisable.

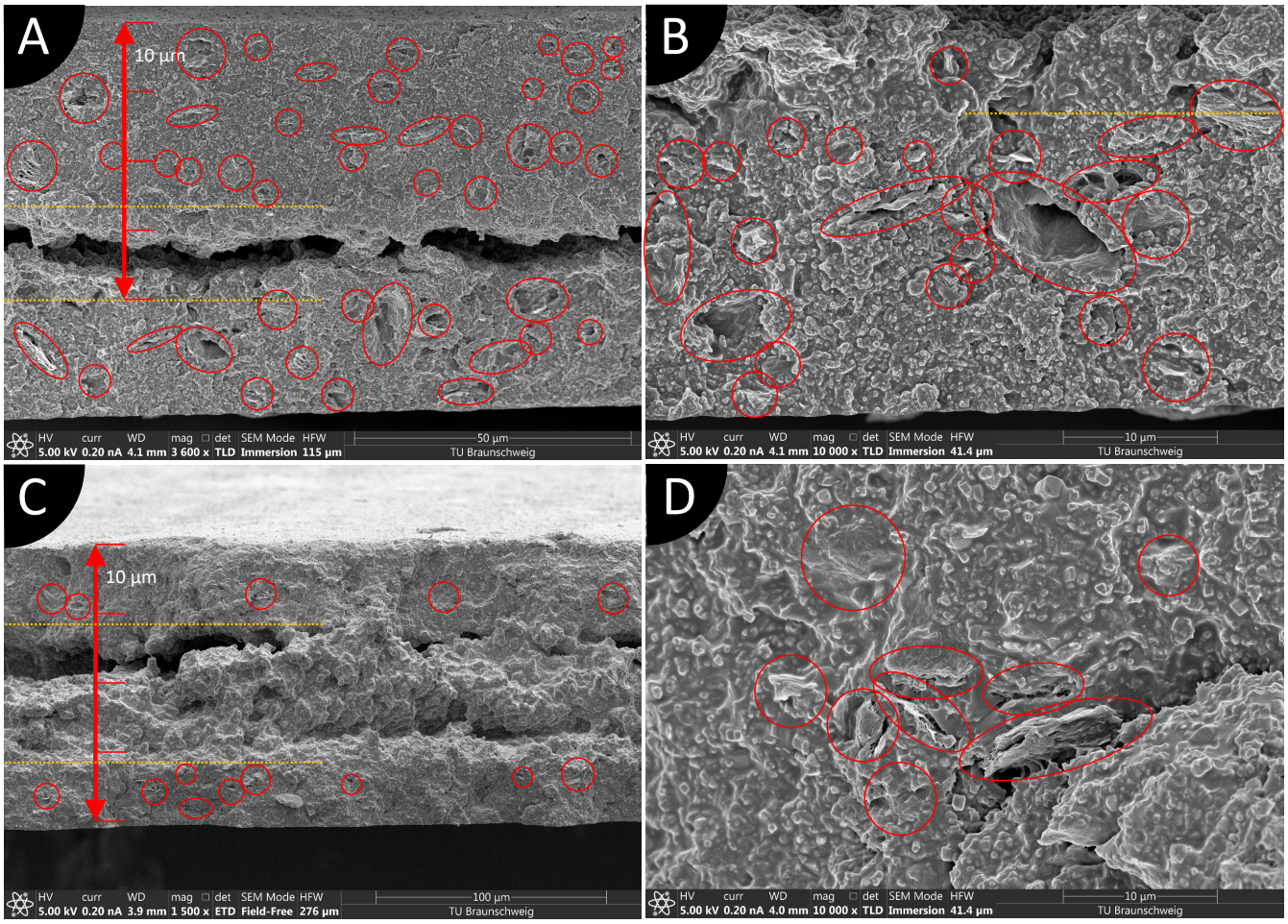

Fig. S26. SEM images of KNN composites with 0.4 wt.% GO3: (A) 30KNN3-0.4GO3 ($\times 3,600$), (B) 30KNN3-0.4GO3 ($\times 10,000$), (C) 30KNN6-0.4GO3 ($\times 1,500$), (D) 30KNN6-0.4GO3 ($\times 10,000$). Orange dashed lines indicate change in photopolymer solidification degree. Red arrow shows depth of cure, gaps between markings are 10 μm. Red circles indicate GO3 where easily recognisable.

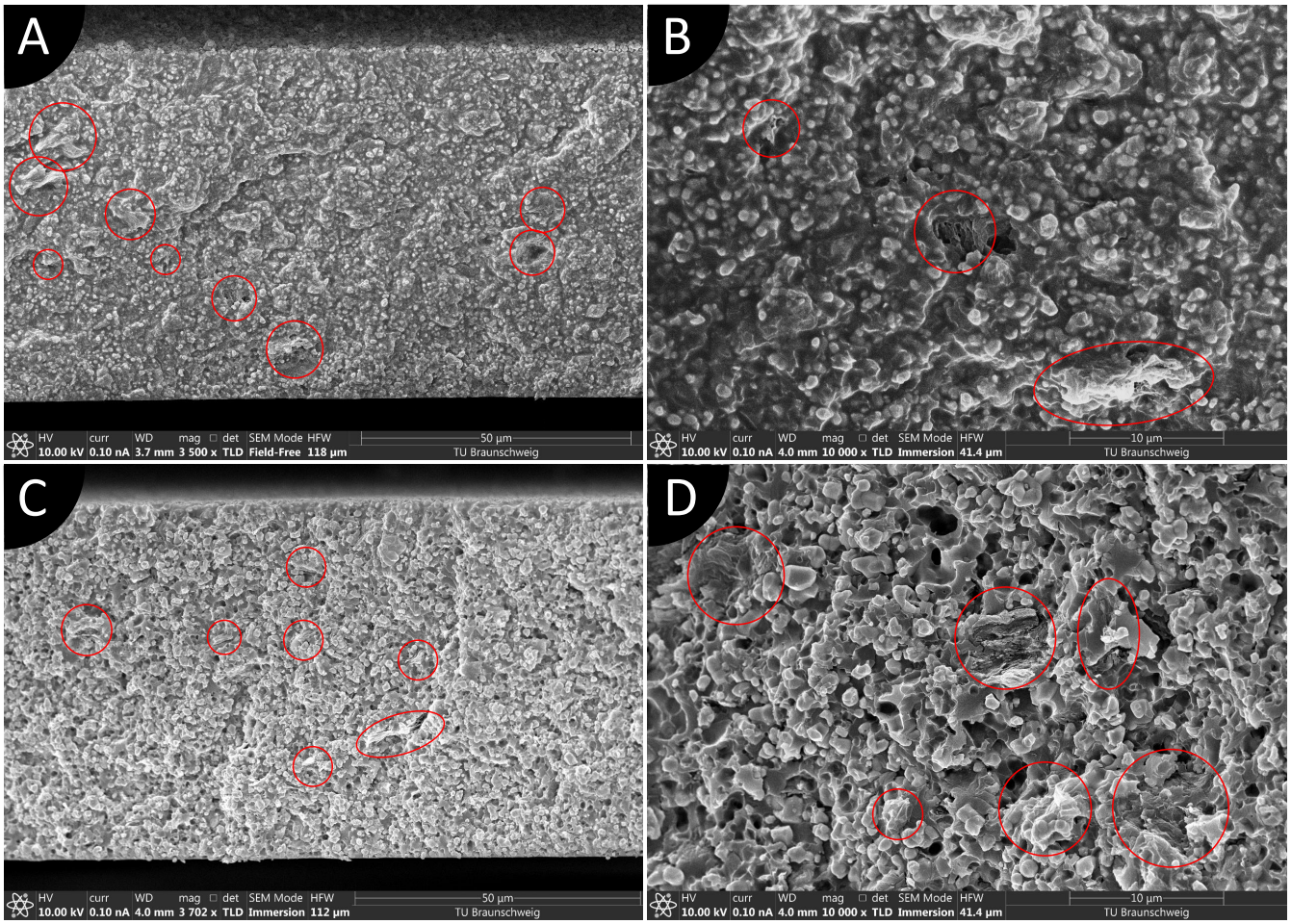

Fig. S27. SEM images of BTO composites with 0.2 wt.% GO3: (A) 30BTO7-0.2GO3 ($\times 3,500$), (B) 30BTO7-0.2GO3 ($\times 10,000$), (C) 30BTO13-0.2GO3 ($\times 3,702$), (D) 30BTO13-0.2GO3 ($\times 10,000$). Red circles indicate GO3 where easily recognisable.

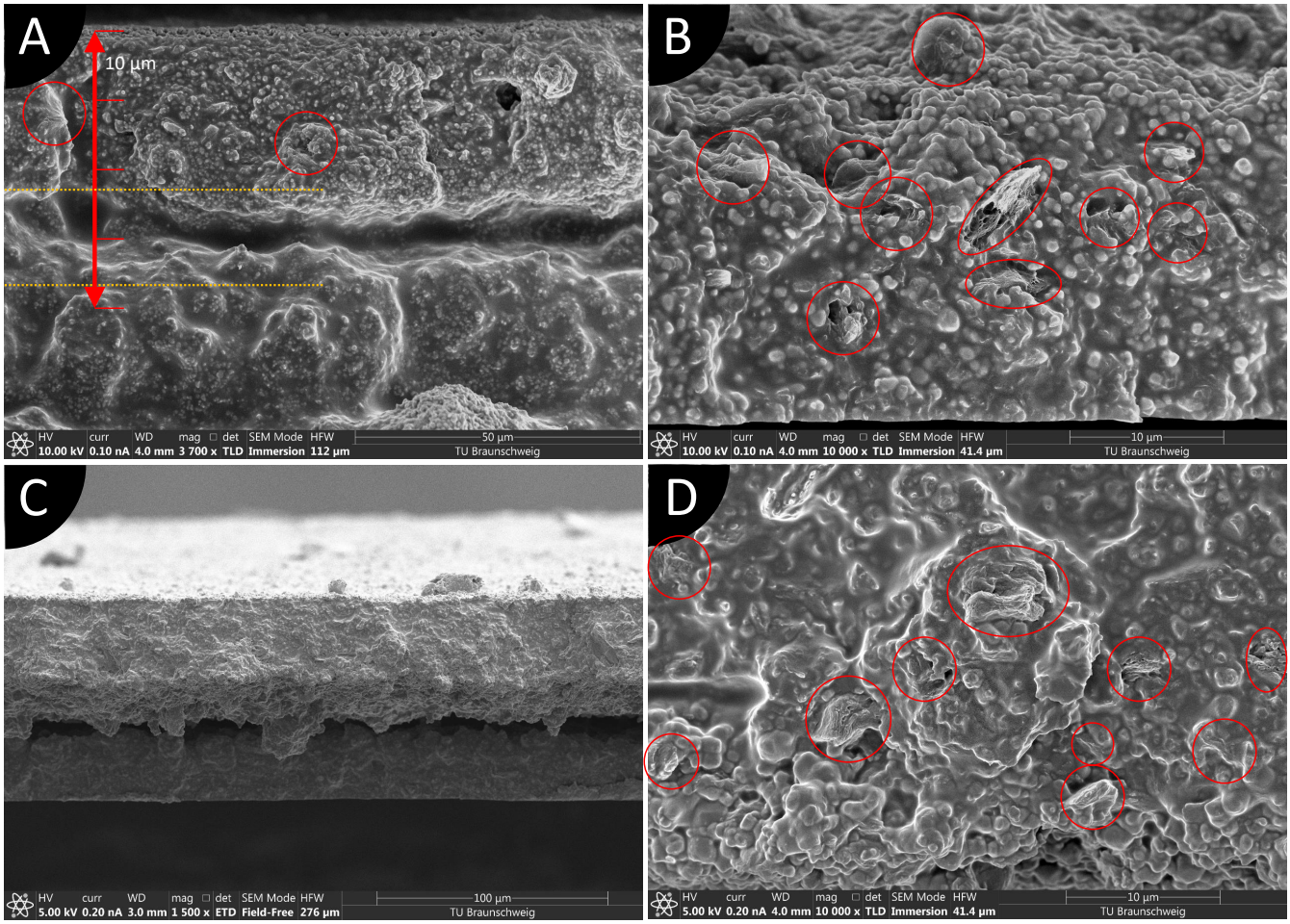

Fig. S28. SEM images of BTO composites with 0.4 wt.% GO3: (A) 30BTO7-0.4GO3 ($\times 3,700$), (B) 30BTO7-0.4GO3 ($\times 10,000$), (C) 30BTO13-0.4GO3 ($\times 1,500$), (D) 30BTO13-0.4GO3 ($\times 10,000$). Orange dashed lines indicate change in photopolymer solidification degree. Red arrow shows depth of cure, gaps between markings are 10 μm. Red circles indicate GO3 where easily recognisable.

Table S3. Properties of piezoelectric composites with measurement errors.

Property	KNN6			BTO13		
	0 wt.% nanofiller	**0.2 wt.% MWCNTs**	**0.2 wt.% GO3**	**0 wt.% nanofiller**	**0.2 wt.% MWCNTs**	**0.2 wt.% GO3**
Thickness, μm	101±13.6	96±11.5	87±11.8	68±2.8	64±4.5	72±1.3
Young's modulus, GPa	2.103±0.189	1.404±0.289	2.046±0.354	2.616±0.08	2.105±0.113	1.952±0.033
Relative permittivity [1]	17.132±1.499	19.321±0.848	18.533±0.958	16.563±0.439	22.529±1.146	19.914±1.225
Dielectric loss [1 2]	0.014	0.039±0.006	0.024±0.004	0.011	0.034±0.005	0.017±0.001
d_{31}, pC/N	-3.805±0.954	-5.586±0.554	-3.925±1.24	-0.607±0.056	-0.227±0.027	-0.465±0.031
g_{31}, V/m [2]	-0.027±0.008	-0.037±0.003	-0.026±0.008	-0.004	-0.001	-0.003
Sensitivity, $(C/m^2)/(m/m)$ [1]	0.0112±0.002	0.0111±0.001	0.0112±0.002	0.0023	0.0007	0.0013

[1] At room temperature, at 1 kHz; [2] If not shown, measurement errors smaller than 0.001.

REFERENCES

1. Umemura, N.; Yoshida, K.; Kato, K., Phase-matching properties of KNbO3 in the mid-infrared. *Applied optics* **1999**, *38*, 991–994. doi:10.1364/AO.38.000991
2. Karvounis, A.; Timpu, F.; Vogler-Neuling, V.V.; Savo, R.; Grange, R., Barium Titanate Nanostructures and Thin Films for Photonics. *Adv. Optical Mater.* **2020**, *8*, 2001249. doi:10.1002/adom.202001249
3. Wemple, S. H.; Didomenico, M.; Camlibel, I., Dielectric and optical properties of melt-grown BaTiO3. *J. Phys. Chem. Solids* **1968**, *29*, 1797–1803. doi:10.1016/0022-3697(68)90164-9
4. Egerton, L.; Dillonu, D. M., Piezoelectric and Dielectric Properties of Ceramics in the System Potassium-Sodium Niobate. *Journal of the American Ceramic Society* **1959**, *42*, 438–442, doi: 10.1111/j.1151-2916.1959.tb12971.x.
5. Bechmann, R., Elastic, Piezoelectric, and Dielectric Constants of Polarized Barium Titanate Ceramics and Some Applications of the Piezoelectric Equations. *The Journal of the Acoustical Society of America* **1956**, *28*, 347–350, doi: 10.1121/1.1908324.
6. Jaffe, H., Piezoelectric Ceramics. *Journal of the American Ceramic Society* **1958**, *41*, 494–498, doi: 10.1111/j.1151-2916.1958.tb12903.x.
7. Qin, Y.; Zhang, J.; Yao, W.; Wang, C.; Zhang, S., Domain Structure of Potassium-Sodium Niobate Ceramics Before and After Poling. *Journal of the American Ceramic Society* **2015**, *98*, 1027–1033, doi: 10.1111/jace.13373.
8. Bomlai, P.; Wichianrat, P.; Muensit, S.; Milne, S. J., Effect of Calcination Conditions and Excess Alkali Carbonate on the Phase Formation and Particle Morphology of Na 0.5 K 0.5 NbO 3 Powders. *J. Am. Ceram. Soc.* **2007**, *90*, 1650–1655. doi:10.1111/j.1551-2916.2007.01629.x
9. Kumar, P.; Pattanaik, M.; Sonia, Synthesis and characterizations of KNN ferroelectric ceramics near 50/50 MPB. *Ceramics International* **2013**, *39*, 65–69. doi:10.1016/j.ceramint.2012.05.093
10. Skidmore, T. A.; Milne, S. J., Phase development during mixed-oxide processing of a [Na 0.5 K 0.5 NbO 3] 1x –[LiTaO 3] x powder. *J. Mater. Res.* **2007**, *22*, 2265–2272. doi:10.1557/jmr.2007.0281
11. Dwivedi, S.; Pareek, T.; Kumar, S., Structure, dielectric, and piezoelectric properties of K 0.5 Na 0.5 NbO 3 -based lead-free ceramics. *RSC Adv.* **2018**, *8*, 24286–24296. doi:10.1039/C8RA04038A
12. Zhu, F.; Skidmore, T. A.; Bell, A. J.; Comyn, T. P.; James, C. W.; Ward, M.; Milne, S. J., Diffuse dielectric behaviour in Na0.5K0.5NbO3–LiTaO3–BiScO3 lead-free ceramics. *Materials Chemistry and Physics* **2011**, *129*, 411–417. doi:10.1016/j.matchemphys.2011.04.032
13. Panomsuwan, G.; Manuspiya, H., A comparative study of dielectric and ferroelectric properties of sol–gel-derived BaTiO3 bulk ceramics with fine and coarse grains. *Appl. Phys. A* **2018**, *124*, 713. doi:10.1007/s00339-018-2126-z
14. Li, X.; Shih, Wei-Heng, Size Effects in Barium Titanate Particles and Clusters. *J. Am. Ceram. Soc.* **1997**, *80*, 2844–2852. doi:10.1111/j.1151-2916.1997.tb03202.x
15. Huang, Kuan-Chih; Huang, Tung-Ching; Hsieh, Wen-Feng, Morphology-controlled synthesis of barium titanate nanostructures. *Inorganic chemistry* **2009**, *48*, 9180–9184. doi:10.1021/ic900854x
16. Maiwa, H., Piezoelectric properties of BaTiO3 ceramics prepared by hot isostatic pressing. *J. Ceram. Soc. Japan* **2013**, *121*, 655–658. doi:10.2109/jcersj2.121.655
17. Huang, Y. Y. and Terentjev, E. M., Dispersion of Carbon Nanotubes: Mixing, Sonication, Stabilization, and Composite Properties. *Polymers* **2012**, *4*, 275–295, doi: 10.3390/polym4010275.
18. Wei, J.; Saharudin, M.S.; Vo, T.; Inam, F., N,N-Dimethylformamide (DMF) Usage in Epoxy/Graphene Nanocomposites: Problems Associated with Reaggregation. *Polymers* **2017**, *9*, 193. doi:10.3390/polym9060193
19. Feng, Z.; Li, Y.; Xin, C.; Tang, D.; Xiong, W. and Zhang, H., Fabrication of Graphene-Reinforced Nanocomposites with Improved Fracture Toughness in Net Shape for Complex 3D Structures via Digital Light Processing. *Journal of Carbon Research* **2019**, *5*, doi: 10.3390/c5020025.
20. Müller, M.T.; Hilarius, K.; Liebscher, M.; Lellinger, D.; Alig, I.; Pötschke, P., Effect of Graphite Nanoplate Morphology on the Dispersion and Physical Properties of Polycarbonate Based Composites. *Materials* **2017**, *10*, 545. doi:10.3390/ma10050545
21. Shuai, C.; Feng, P.; Gao, C.; Shuai, X.; Xiao, T.; Peng, S., Graphene oxide reinforced poly(vinyl alcohol): nanocomposite scaffolds for tissue engineering applications. *J RSC Adv.* **2015**, *5*, 25416–25423, doi: 10.1039/C4RA16702C.
22. Payo, I.; Hale, J. M., Dynamic characterization of piezoelectric paint sensors under biaxial strain. *Sensors and Actuators A: Physical* **2010**, *163*, 150–158. doi:10.1016/j.sna.2010.08.005
23. Mitkus, R.; Taleb A.A.; Sinapius, M., An Attempt to Topology Optimize 3D Printed Piezoelectric Composite Sensors for Highest D31 Output. *Proceedings of the ASME 2021 Conference on Smart Materials, Adaptive Structures and Intelligent Systems. ASME 2021 Conference on Smart Materials, Adaptive Structures and Intelligent Systems. Virtual, Online.* **September 14–15, 2021**. doi:10.1115/SMASIS2021-68029
24. Kok, S. L.; Lau, Kok-Tee; Ahsan, Q., Substrate-Free Thick-Film Lead Zirconate Titanate (PZT) Performance Measurement Using Berlincourt Method. *Advanced Materials Research* **2014**, *895*, 204–210, doi: 10.4028/www.scientific.net/AMR.895.204.